

Copy

203,515

~~CONFIDENTIAL~~

RM A55G20

USAF TECHNICAL LIBRARY  
FOLLOWING INFORMATION  
ALAN C. ...

12 OCT 1955

TECH LIBRARY KAFB, NM  
0143364

NACA

# RESEARCH MEMORANDUM

TEMPERATURE RECOVERY FACTORS ON A SLENDER  $12^\circ$   
CONE-CYLINDER AT MACH NUMBERS FROM 3.0 TO  
6.3 AND ANGLES OF ATTACK UP TO  $45^\circ$

By John O. Reller, Jr., and Frank M. Hamaker

Ames Aeronautical Laboratory  
Moffett Field, Calif.

CLASSIFIED BY ... TO UNCLASSIFIED ...  
NASA Tech Pub Announcement #44  
(OFFICER AUTHORIZED TO CHANGE)

By ...  
NAME AND

... NK ...  
GRADE OF OFFICER MAKING CHANGE)

... 17 Feb 61 ...  
DATE

CLASSIFIED DOCUMENT

This material contains information affecting the National Defense of the United States within the meaning of the espionage laws, Title 18, U.S.C., Secs. 793 and 794, the transmission or revelation of which in any manner to an unauthorized person is prohibited by law.

## NATIONAL ADVISORY COMMITTEE FOR AERONAUTICS

WASHINGTON

October 3, 1955

~~CONFIDENTIAL~~

NACA RM A55G20

6462



0143364

P  
NACA RM A55G20~~CONFIDENTIAL~~

## NATIONAL ADVISORY COMMITTEE FOR AERONAUTICS

RESEARCH MEMORANDUMTEMPERATURE RECOVERY FACTORS ON A SLENDER  $12^\circ$ 

CONE-CYLINDER AT MACH NUMBERS FROM 3.0 TO

6.3 AND ANGLES OF ATTACK UP TO  $45^\circ$ 

By John O. Reller, Jr., and Frank M. Hamaker

## SUMMARY

Recovery temperatures were measured on a slender cone-cylinder, having a  $12^\circ$  vertex angle and a 1.25-inch-diameter cylinder, at Mach numbers from 3.02 to 6.30. The angle-of-attack range was  $0^\circ$  to  $45^\circ$  at Mach numbers up to 3.50,  $0^\circ$  to  $25^\circ$  at Mach number 4.23, and  $0^\circ$  to  $15^\circ$  at Mach numbers from 5.04 to 6.30. The free-stream Reynolds numbers varied from  $1.8 \times 10^6$  to  $11.0 \times 10^6$  per foot. A transverse cylinder of the same diameter was also tested at 3.02 Mach number. At angles of attack up to  $10^\circ$ , the temperature distribution varied in a complex manner apparently in response to changes in the location and extent of the boundary-layer transition region. For larger angles, the effects of adiabatic compression and flow separation became prominent; resultant recovery factors based on free-stream conditions ranged from 6 percent above to 7 percent below those measured at zero angle of attack. A circumferential recovery-temperature pattern similar to that for a transverse cylinder was developed on the cylindrical afterbody at angles of attack greater than  $25^\circ$ . In the high Reynolds number range of this investigation, the average recovery factor (based on free-stream conditions) for the entire surface did not exceed that for zero angle of attack by more than 1 percent for angles of attack up to  $35^\circ$ .

Recovery factors based on local stream conditions for laminar boundary-layer flow, at zero angle of attack, were in agreement with the square root of the Prandtl number based on wall temperature, while for turbulent flow the cube root of the Prandtl number established an upper limit. Compared to the predictions of Van Driest, Young and Janssen, and Tucker and Maslen, the laminar boundary-layer data at Mach numbers greater than 4 were about 1 percent low and the turbulent boundary-layer data were high by about the same percentage. With increasing angle of attack, recovery factors (based on local flow conditions) on the windward meridian of the conical nose gradually decreased, dropping at  $45^\circ$  to as much as 6 percent below the zero-angle-of-attack value. No significant variation of

~~CONFIDENTIAL~~~~CONFIDENTIAL~~

recovery factor with either Mach number or Reynolds number was observed, in regions of either laminar or turbulent boundary-layer flow, for the range of conditions of this investigation.

## INTRODUCTION

Aerodynamic heating is one of the foremost considerations in the design of aircraft for flight at high supersonic speeds. The recovery temperature is a controlling factor in the heating phenomenon since the rate of heat transfer is proportional to the difference between this temperature and the actual surface temperature. The prediction of recovery temperatures for a body of revolution at angle of attack is of particular interest because this shape often constitutes a major component of supersonic aircraft. At present there is little theoretical information on this problem, and existing experimental data (refs. 1 and 2) are available only over a limited Mach number and angle-of-attack range.

The purpose of this investigation is, then, to provide experimental values of temperature recovery factors on a slender body of revolution at angles of attack from zero to  $45^\circ$  and at Mach numbers from 3.0 to 6.3. Experimental recovery-factor data for the limiting case of a cylinder inclined  $90^\circ$  to the flow are also presented. The more significant results of the investigation are discussed briefly and, with the aid of several flow visualization methods, are related to boundary-layer phenomena.

## NOTATION

a	speed of sound, ft/sec
$C_p$	surface pressure coefficient, $\frac{p_e - p_\infty}{q_\infty}$ , dimensionless
$c_p$	constant-pressure specific heat, BTU per pound, $^\circ\text{F}$
g	acceleration of gravity, ft/sec <sup>2</sup>
k	coefficient of thermal conductivity, BTU per second, sq ft, $^\circ\text{F}/\text{ft}$
M	Mach number, $\frac{V}{a}$ , dimensionless
N	reciprocal of exponent defining boundary-layer velocity profile, dimensionless
$N_{Pr}$	Prandtl number, $\frac{g c_p \mu}{k}$ , dimensionless

p	static pressure, lb/sq ft
p <sub>t</sub>	stagnation pressure, lb/sq ft
q	dynamic pressure, $\frac{\rho V^2}{2}$ , lb/sq ft
R	Reynolds number, $\frac{V_{\infty} \rho_{\infty} x}{\mu_{\infty}}$ , dimensionless
S	surface area of model, sq ft
T	absolute temperature, °R
V	resultant velocity, ft/sec
x	distance along surface measured from model tip, in.
α	angle of attack, deg
η <sub>r</sub>	temperature recovery factor, $\frac{T_e - T}{T_t - T}$ , dimensionless
η <sub>r,av</sub>	average recovery factor for entire model surface, $\frac{1}{S} \int \eta_{r,\infty} dS$ , dimensionless
θ	circumferential angle measured from windward meridian line, deg
μ	absolute viscosity, lb-sec/sq ft
ρ	mass density, slugs/cu ft

## Subscripts

t	stagnation condition
∞	free-stream condition at a location in the test section corresponding to the midpoint of a test model
l	local condition adjacent to the body at the outer edge of the boundary layer
e	local condition at the surface of an insulated body in thermal equilibrium

## EQUIPMENT AND TEST PROCEDURE

## Wind Tunnel and Auxiliary Equipment

The experimental data of this investigation were obtained in the Ames 10- by 14-inch supersonic wind tunnel at Mach numbers from 3.0 to 6.3. This tunnel is supplied with dry air at pressures up to 6 atmospheres absolute. At Mach numbers above 4.2 the supply air is heated to prevent air condensation in the test section. Details of the construction, operating range, and calibration of the wind tunnel may be found in reference 3.

A center-of-curvature-type schlieren apparatus and a simple shadow-graph system were used interchangeably to make visual studies of the flow about models. Additional visual evidence was obtained with the vapor-screen technique described in reference 4 and the china-clay method (ref. 5).

## Test Bodies and Instrumentation

The basic body of this investigation was a  $12^\circ$  included angle cone-cylinder combination of over-all fineness ratio 12. This shape was chosen because it is relatively simple, hence enabling some comparison between theory and experiment. Temperatures and pressures were measured with separate models. A cylinder with a length-to-diameter ratio of 5-1/2 was used to obtain temperature data in the limiting case of  $90^\circ$  angle of attack.

Temperature models and measuring equipment.- The recovery temperature was measured on a model of the basic body made of a free-machining stainless steel. Except for an inaccessible region near the tip and a support adapter at the base, the wall thickness was a uniform 0.025 inch. With this thin wall, the heat capacity of the model and the heat conduction within the shell were minimized. Thirty copper-constantan duplex thermocouple wires were soldered into holes through the surface in a plane passing through the axis of symmetry (meridian plane) as shown in figure 1(a). The outer surface of the model was then polished to a finish of about 10 microinches. A thin layer ( $< 0.0005$  inch) of hard chromium was electroplated on the surface and the model was again polished to the same finish. The result was a highly polished and durable surface (see fig. 2).

The cylinder model had a shell thickness of 0.013 inch (see figs. 1(b) and 2) and was constructed in the same manner as the cone-cylinder. Twenty-four thermocouples were distributed along two opposing elements of the cylinder and in two circumferential planes as shown in figure 1(b).

The output voltages of all model thermocouples were measured on a recording, self-balancing potentiometer.

The cone-cylinder model was supported from the base by various double-bent stings which positioned the midpoint of the model on the wind-tunnel center line at approximately the same axial station for all angles of attack. The crossflow cylinder was held at both ends in a forklike support. Typical support assemblies are shown in figure 3.

Reservoir temperatures were indicated by 19 copper-constantan thermocouples distributed, in one plane, over the cross-section area of the wind-tunnel settling chamber. Output voltages of these thermocouples were measured on an indicating, self-balancing potentiometer.

To evaluate the effect on test-section total temperature of heat transfer at Mach numbers 5.0 and 6.3 from the heated air stream to the tunnel walls, especially in the vicinity of the minimum section, a shielded total temperature probe similar to that of reference 6 was used. The body of the probe was stainless steel, while the hemispherical support was micarta and the thermocouple lead was temperature-insulated. Thermocouple voltage was measured with a manually operated precision potentiometer. No effect of heat transfer on test-section total temperature was indicated, there being negligible difference between the measured total temperature and the average reservoir temperature.

Pressure model and measuring equipment.- The surface pressures were measured on a model of the cone-cylinder similar in construction to that used for the temperature measurements. Wall thickness was a uniform 0.025 inch, and thirty 0.040-inch-diameter pressure orifices were spaced along opposite meridian lines in the same locations as shown in figure 1(a). Pressures above 7 centimeters of mercury were measured on conventional U-tube mercury manometers, while lower pressures were measured with McLeod type mercury manometers. Reservoir pressure was measured with a sensitive Bourdon type pressure gage; static and dynamic pressures in the test section were determined from wind-tunnel calibration data and the reservoir pressure.

Pressures were not measured on the transverse cylinder inasmuch as representative data were obtainable from other sources (see, e.g., ref. 7).

#### Test Procedure

Model surface temperatures at each test condition were continuously recorded until the difference between successive readings for all thermocouples was equal to or less than the repeatability of the recording equipment. At this time several sets of equilibrium data were taken. Likewise, model surface pressures were observed at short intervals of

~~CONFIDENTIAL~~

time until the difference between successive readings was within the measuring accuracy. Equilibrium pressures were then recorded.

Data were obtained in several meridian planes by rotating the test model relative to its support. Wind-tunnel flow blockage was the limiting factor in high angle of attack, high Mach number operation. Data were obtained at angles of attack up to  $15^\circ$  for all test Mach numbers, up to  $25^\circ$  for Mach numbers of 3.02 through 4.23, and up to  $45^\circ$  for Mach numbers of 3.02 and 3.50 only. Testing of the  $90^\circ$  crossflow cylinder was restricted to  $M_\infty = 3.02$ . Free-stream Reynolds numbers varied from  $1.8 \times 10^6$  to  $11.0 \times 10^6$  per foot. A summary of the test conditions for models with polished surfaces is given in tables I and II.

Limited temperature data were obtained with the cone-cylinder model for two types of surface roughness, one type being a distributed roughness of the order of 0.0003 inch in height and the other a localized roughness consisting of two 0.020-inch-diameter wire rings (1/4-inch spacing) about 1/2 inch from the tip of the model.

## INTERPRETATION AND ACCURACY OF TEST RESULTS

### Interpretation of Visual Evidence

Spark shadowgraph pictures (5-microseconds exposure) were taken in the  $\theta = 0^\circ$  and  $180^\circ$ , and  $90^\circ$  and  $270^\circ$ , planes to aid in the analysis of the surface temperature and pressure measurements. Boundary-layer condition, whether laminar or turbulent, and the approximate location of the transition region were determined from these pictures. Although some evidence of the character of flow in separated regions could also be deduced, better definition of separated flow was obtained in a similar set of schlieren photographs (6-milliseconds exposure). To provide additional information on the region of separated flow, two other visual methods, the vapor-screen technique and the china-clay method, were employed.

### Reduction of Temperature Data

The measured surface temperatures are presented in the form of temperature recovery factors based on either free-stream or local flow conditions. Preference is given to recovery factors based on free-stream conditions,  $\eta_{r,\infty} = \frac{T_e - T_\infty}{T_t - T_\infty}$ , since they provide a direct measure of surface temperatures in separated as well as nonseparated flow regions and are not influenced by the errors inherent in the determination of local flow conditions. The assumption is made that surface temperatures are essentially the same as would exist on a perfectly insulated body in thermal

~~CONFIDENTIAL~~

equilibrium. Deviations from this assumed condition are discussed in the section on accuracy of results. Local recovery factors,  $\eta_{r,l} = \frac{T_e - T_l}{T_t - T_l}$ , are used primarily to evaluate the effect of angle of attack on local boundary-layer temperature conditions in regions of nonseparated flow and to provide a basis for comparison of the data of these tests with those of previous investigations.

The determination of local recovery factor requires a knowledge of local Mach number. Local Mach numbers around the conical nose were determined by the following method: The ratio of stagnation pressures across the nose shock wave in the  $\theta = 0^\circ$  plane was calculated from a measurement of the shock-wave angle taken from a shadowgraph picture. This ratio was used in conjunction with the measured wind-tunnel stagnation pressure and surface static pressures to calculate the local Mach number distribution.<sup>1</sup> This method is known to be applicable in regions of nonseparated flow.

#### Reduction of Pressure Data

Surface pressure measurements are presented in the form of pressure coefficients where free-stream static and dynamic pressures were taken from the wind-tunnel calibration data (ref. 3). The free-stream static pressure used was that of the undisturbed stream at the location of the model surface pressure orifice, while the dynamic pressure corresponded to the undisturbed stream value at the location of the midpoint of the model.

#### Accuracy of Test Results

The model support system was calibrated for deflection by applying static loads to simulate estimated lift forces. The resultant uncertainty in angle of attack is estimated to be  $\pm 0.1^\circ$ . The longitudinal location of the boundary-layer transition region from shadowgraph pictures generally is known within  $\pm 1/2$  inch, while the location of separation by the china-clay method is estimated with an absolute error in circumferential angle of less than  $\pm 8^\circ$ .

Model surface pressures and wind-tunnel stagnation pressures were measured with an error of less than  $\pm 1$  percent, while free-stream static and dynamic pressures (from wind-tunnel calibration data) are of similar precision. A small additional uncertainty is inherent in the pressure

---

<sup>1</sup>This calculation derives from the fact that for this body the entropy on the surface just outside the boundary-layer is essentially constant and equal to the entropy in the plane  $\theta = 0^\circ$  (see, e.g., ref. 8).

---



data, since no correction was made for stream angle or Mach number gradients in the test region. As a result, the estimated error in pressure coefficient varies with the magnitude of the measured surface pressure and, to a lesser extent, with the free-stream Mach number. Thus, in the vicinity of the highest measured surface pressures (high angles of attack in the low Mach number range), the probable error in pressure coefficient for all test conditions does not exceed  $\pm 0.014$ . The corresponding error in the low pressure range is  $\pm 0.004$ . These values are in general somewhat high since with increasing free-stream Mach number the probable error decreases to about half the foregoing estimates.

The precision of the calculated local Mach number is dependent on the accuracy of both surface-pressure and shock-wave-angle measurement. On this basis the probable error in local Mach number is  $\pm 0.03$ .

The accuracy of recovery factors based on free-stream conditions is influenced by the variation of Mach number in the test section, the uniformity and stability of settling-chamber temperatures, the precision with which temperature measurements were made, and the local heat conduction through the model shell. The probable error in free-stream recovery factor from the first three sources is  $\pm 0.3$  percent. The effect of shell conduction on the accuracy of free-stream recovery factors will, in all likelihood, be most pronounced in those areas where aerodynamic heat-transfer rates are relatively low. A numerical analysis of the conduction effect in regions of low velocity flow (low heat-transfer rates), such as near the  $\theta = 0^\circ$  meridian at high angles of attack and in separated flow, indicated that the most critical locations are those where large changes of temperature gradient occur and where temperatures are at a maximum or minimum. Thus, the most severe case encountered in this investigation was in the vicinity of the stagnation point on the transverse cylinder. At this location the experimental data, which are in good agreement with the results of the numerical analysis, indicate a conduction error of about 1.2 percent (the deviation from  $\eta_{r,\infty} = 1.00$ ) in the measured recovery factor. Similarly, the substantial temperature gradient changes that occur on the cone-cylinder model at  $\alpha > 15^\circ$  can introduce errors of almost 1 percent in the vicinity of the  $\theta = 0^\circ$  meridian. The estimated errors at smaller angles of attack and in separated flow regions are less than 1/2 percent as the result of shell conduction. Thus, while in certain localized regions free-stream recovery factors may be subject to a probable error from all sources of about 1 percent, in general, the probable error is about 1/2 percent.

Recovery factors based on local flow conditions are subject to an additional error in the determination of the local Mach number. However, it is demonstrated in figure 4 that a sizable relative error in local Mach number will reflect a small relative error in local recovery factor, and further, that this error is reduced as the Mach number increases. The effect of shell conduction on local recovery factors is also illustrated in figure 4 where it is seen that errors can be sizable in localized

regions of maximum or minimum temperatures. Except for this shell conduction error at large angles of attack, the probable error in local recovery factor is less than  $\pm 1$  percent.

## PRESENTATION OF RESULTS

### Visual Evidence

The photographs presented in figures 5 through 8, for  $M_\infty = 3.02$ , are representative of the results obtained with the four flow-visualization methods used in this investigation. Figure 5 is a group of shadowgraph pictures which shows the location of boundary-layer transition in the  $\theta = 0^\circ$  and  $180^\circ$  plane on the cone-cylinder model. Figure 6 is a similar group of schlieren photographs which illustrates the character of flow separation regions. The circumferential location of the flow-separation line is seen in the china-clay photographs of figure 7, while the vapor-screen photographs of figure 8 show flow separation in a plane perpendicular to the wind-tunnel axis. Note that parts (a) through (c) of figure 8 are photographs of the flow taken from a downstream location, while part (d) is a view from an upstream position.

### Temperature Distributions

The main body of recovery temperature data is presented in figures 9 through 13 as a function of longitudinal and circumferential position on the model. Unless otherwise stated, all the data shown in these and the subsequent figures are for the basic cone-cylinder shape and are based on free-stream conditions. Figures 9 and 10 show the longitudinal variation of free-stream recovery factor on the  $\theta = 0^\circ$  and  $180^\circ$  meridian lines for all Mach numbers over the angle-of-attack range (to retain clarity, the data at large angles of attack are shown separately in fig. 10). Representative variations of  $\eta_{r,\infty}$  along other meridians are shown in figure 11, while circumferential distributions of  $\eta_{r,\infty}$  at selected cross sections appear in figure 12. (It will be noted that fig. 12 presents data which are not shown in fig. 11.) The results for the transverse cylinder are plotted in figure 13.

Figures 14, 15, and 16 illustrate some effects of stream Reynolds number and Mach number on recovery factor, and figure 17 shows the effect of model surface finish and isolated roughness elements on recovery factor.

### Pressure Distributions

Representative pressure data are shown in figures 18 and 19 for the cone-cylinder model at a free stream Mach number of 3.02. Pressure

coefficient is given as a function of  $\theta$  both on the cone and at the midpoint of the cylindrical afterbody for angles of attack up to  $25^\circ$ . Comparison is made with the second-order theory of Stone (refs. 9 through 12) and the inclined-body approximation of Allen (ref. 4).

### Summary Figures

Figure 20 presents the location of the end of boundary-layer transition as a function of angle of attack at Mach numbers from 3.02 to 4.23. Two independent sets of data are shown on the figure; one set was obtained from the longitudinal recovery-factor patterns of figures 9 and 10, while the other was taken from a series of shadowgraph pictures similar to those of figure 5. No curves have been faired through the data, since this figure is used only to illustrate general trends. Figure 21 presents the estimated circumferential angle of flow separation at the midpoint of the cylindrical afterbody as a function of angle of attack. This information provides the basis for a qualitative correlation of temperature-distribution patterns with flow separation. Separation points were determined from china-clay photographs similar to those of figure 7 and from surface-pressure distributions. The latter data are the result of comparisons between experimental and theoretical pressure distributions as illustrated, for example, by figures 18 and 19. Specifically, a deviation of the experimental trend from the trend of the theoretical curve (i.e., a decreasing rate of lee-side pressure recovery) was assumed to indicate the approximate location of flow separation.

Recovery factors at two axial locations, one on the cone and one on the cylindrical afterbody, are shown as a function of angle of attack in figure 22, while in figure 23 an average recovery factor (area-weighted average for entire surface) is presented.

The variation of local Mach number on the cone with angle of attack and circumferential location is given in figure 24 for a free-stream Mach number of 3.50. Local Mach numbers computed from surface pressures and nose shock-wave measurements are compared with those predicted by the Stone theory.

Recovery factors based on local stream conditions are given in figures 16, 25, and 26. Figure 16 shows the variation of local recovery factor with axial location on the model, at zero angle of attack, for regions of laminar-boundary-layer flow. In figure 25, local recovery factor on the cone is plotted as a function of angle of attack and circumferential location for  $M_\infty = 3.50$ . Local Mach number is the independent variable in figure 26, where the zero-angle-of-attack data of this investigation are compared with theoretical predictions.

## DISCUSSION OF RESULTS

Recovery temperature is obtained on an insulated surface when a balance is reached between the generation of heat, due to viscous dissipation and compression of air, and the removal of heat by conduction and convection within the boundary layer. (Radiant heat transfer is presumed negligible.) It might be expected, then, that the recovery temperature would be considerably altered by large boundary-layer changes such as occur over the angle-of-attack range of this investigation. The temperature recovery factors did, in fact, vary substantially with angle of attack, exhibiting a behavior that was apparently a response to several distinct phenomena. In the following discussion consideration is given to some of these phenomena.

## Recovery Factors Based on Free-Stream Conditions

Small angles of attack.- Temperature recovery factors on the forepart of the model at angles of attack from  $1^\circ$  to  $5^\circ$  are markedly higher than at zero angle of attack as seen in figure 9. This result is rather surprising and to some extent the reasons for it are not understood. It has been observed in previous investigations, however, that transition on the leeward side of a body moves forward with increasing angle of attack. This movement of transition is very likely due to the upwash of low-kinetic-energy boundary-layer air from the windward side. Although the data of this investigation show a similar forward movement of transition (see fig. 20) it is not at all clear that the effect of upwash could be so pronounced at small  $\alpha$ , say  $1^\circ$  or  $2^\circ$ . The windward side recovery-factor rise is thought to be due, in part, to a forward movement of transition as a result of contamination from the lee-side turbulent boundary layer, with turbulence spreading circumferentially as it is washed downstream after the manner proposed in reference 13.<sup>2</sup> (Note that the calculated effect of heat conduction through the model shell is much smaller than this observed recovery-factor rise.) Aside from the effect of transition movement, there is an apparent increase of recovery temperature in regions of predominantly laminar flow, as seen in figure 10(e) over the first 6 inches of the model. A small portion of this increase could result,

---

<sup>2</sup>Except for  $M_\infty = 3.02$ , this effect is not seen in the transition data of figure 20, where the change in appearance of the boundary layer on shadowgraph pictures is compared, as to location, with the end of the transition region determined from longitudinal recovery-factor distributions. The difference between the trend of figure 20 and that discussed here is attributed to the "stretching out" of the transition zone as mentioned in the next paragraph. For further discussion of transition see a later section entitled "Correlation of Temperature Patterns With Boundary-Layer Transition and Separation."

---

of course, from the change in local Mach number; the remainder is not understood. A similar behavior is shown by the data of reference 2.

Coupled with this observed increase of recovery factor in the laminar region and the apparent forward movement of the start of transition is a considerable "stretching out" of the transition zone on the windward side of the body. This is most clearly shown in figure 9(c) where the change of slope of the curves and the rearward movement of the point of maximum recovery factor with increasing angle of attack can be seen. This delay of transition to fully turbulent flow probably results from the removal of low-kinetic-energy boundary-layer air from the vicinity of the  $\theta = 0^\circ$  meridian by the cross component of the flow.

Large angles of attack.- As the angle of attack approaches  $10^\circ$ , there is a tendency for recovery factors along the windward side of the body to decrease (e.g., fig. 10(a)). This is attributed to a return to more nearly laminar flow as the influence of crossflow boundary-layer removal becomes more pronounced. As the angle is increased beyond  $10^\circ$ , recovery factors on the windward side begin to rise as a result of adiabatic compression.

The recovery-factor distribution around the model follows no obvious pattern for angles of attack below  $15^\circ$ , because of the relatively large influence of transitional boundary-layer flow (see fig. 12). It will be noted, however, that in some cases lee-side recovery factors approaching the base of the model are as much as 0.02 to 0.05 higher than the opposite side at  $\alpha = 10^\circ$ . (In ref. 1 this effect was attributed to the proximity of vortex centers in the separated flow.) At angles of attack of about  $15^\circ$  there appear circumferential distributions in which the maximum recovery factor is on the windward meridian and the minimum is on the lee meridian of the model. For angles of attack above  $25^\circ$  these characteristic patterns evolve into a distribution similar to that obtained on the transverse cylinder, namely, that the minimum value occurs in the vicinity of the separation line as shown in figures 12(a) and 12(b).

Figure 22 summarizes the variation of windward and leeward recovery factors with angles of attack to  $45^\circ$ . To retain clarity, only representative curves are shown. Recovery factors at angles of attack to  $10^\circ$  are generally from 1 to 4 percent higher than those at the same location at  $\alpha = 0^\circ$ . As angle of attack is increased to  $45^\circ$ , windward-side recovery values rise to about 0.95. In contrast, lee-side values reach minimums at  $\alpha = 25^\circ$  to  $35^\circ$  which are as much as 5 percent below those at  $\alpha = 0^\circ$ , with a subsequent increase at larger angles of attack.

For the limiting case of  $\alpha = 90^\circ$  (see fig. 13) a recovery factor of about 0.99 was measured on the stagnation line (as shown earlier, shell conduction in this critical region caused the deviation from  $\eta_{r,\infty} = 1.00$ ) while a minimum of about 0.89 occurred in the vicinity of  $\theta = 90^\circ$ . Although the lee-side values of the present investigation were considerably higher than those reported in reference 7, (respectively, 0.95 and 0.89 at

$\theta = 160^\circ$ ), a significant difference between the two tests was the Reynolds number, which was larger by a factor of 8 in the present investigation.

The average recovery factors plotted in figure 23 are area-weighted values which summarize the effect of angle of attack on the temperature level of the entire body.<sup>3</sup> It is apparent that the variations previously discussed are of sufficient magnitude to affect the over-all trend. Thus, for angles of attack up to  $10^\circ$ , the effect of lee-side temperature rise disappears at Mach numbers above 3.50 (generally decreased Reynolds number) and the small-angle laminar-boundary-layer effect becomes predominant. For  $10^\circ < \alpha < 25^\circ$  there is a general decrease of average recovery factor which, in the low Mach number range (high Reynolds number), results in minimum values which are less than the averages at  $\alpha = 0^\circ$  and which do not exceed the zero-angle values for angles of attack up to  $35^\circ$ .

Effect of Reynolds number and surface roughness.- The Reynolds number effects encountered in this investigation were, in the main, evidenced by changes in the location and extent of the boundary-layer transition region. These effects were not confined to the windward side of the body but were, to a lesser extent, also shown in regions of separated flow on the lee side. In a sample comparison shown in figure 14, a reduction in Reynolds number from 11.0 to 4.2 million per foot lowered windward meridian recovery factors by about 2 to 4 percent, primarily as a result of the aft movement of the transition region. Corresponding leeward values dropped from 1 to 2 percent. This feature was also noted in the comparable transverse-cylinder data of figure 13, as mentioned in the previous section. Other effects of Reynolds number include a small decrease of recovery factor with length of run that was characteristic of both laminar and turbulent flow, and, as shown for example in figure 15, an increased length of run in the transition region in response to a reduction in stream Reynolds number. The data also appear to show that, for laminar-boundary-layer flow, larger recovery-factor variations occurred in the low Reynolds number range of this investigation in response to Mach number changes. An example of this effect is presented in figure 16, where recovery factors on the forepart of the model show a pronounced Mach number response at  $R = 4.2$  million per foot, compared to the small change at  $R = 8.6$  million per foot. This could be due, in part, to a decrease of effective surface roughness as a result of increasing boundary-layer thickness with Mach number. Further investigation is necessary to establish the extent of this influence in low Reynolds number flows.

The effect of surface roughness on recovery factor is shown in figure 17. The square symbols represent recovery factors for a surface with distributed roughness elements of the order of 0.0003 inch in height, while the diamond symbols are data for a localized roughness consisting of two 0.020-inch-diameter wire rings (1/4-inch spacing) located about 1/2 inch from the tip of the model. Comparison of these results with the

<sup>3</sup>Angles of attack from  $1^\circ$  to  $4^\circ$  are omitted because of insufficient data.

~~CONFIDENTIAL~~

data obtained with the polished surface shows, as expected, that roughness causes a forward movement of transition at both  $\alpha = 0^\circ$  and  $15^\circ$ . The effects of roughness are similar for both  $0^\circ$  and  $15^\circ$  angle of attack, although the recovery-factor rise is somewhat less pronounced at  $\alpha = 15^\circ$  for  $M_\infty = 4.23$  and  $5.04$ . There are indications that roughness may lower recovery factors in turbulent regions, in particular as shown in figure 17(a). It also tends to "wash out" the distinctive sharp temperature rise normally associated with the transition region. An interesting feature is noted in figures 17(b) and (c), where the decrease of recovery factor for a short distance downstream of the localized roughness suggests that the disturbance introduced by the roughness is partially damped by the boundary layer and that transition is completed some distance downstream. This behavior is in agreement with the experimental results reported in reference 14, where it is shown that roughness elements smaller than a critical size promote transition in regions downstream of the element location, rather than at the element.

#### Correlation of Temperature Patterns With Boundary-Layer Transition and Separation

The recovery temperatures on a body of revolution at angle of attack have been stated to be significantly dependent upon several characteristics of the boundary-layer flow. The location and extent of boundary-layer transition, the upwash of air of low kinetic energy from windward to leeward side, the location of the flow separation point, and the phenomena associated with the separated flow are several of the more important features that have been mentioned. The observed recovery-factor variations have been related to these features by the four flow-visualization methods.

Boundary-layer transition.- For the most part, transition effects have been related to the observed temperature patterns in the previous discussion. The general trend of longitudinal transition location with angle of attack has, however, received only passing mention. Now, it is recognized that boundary-layer transition is not a stationary phenomenon; in fact, there is ample experimental evidence that it is a time-dependent composite of a large number of turbulent "bursts." Consequently, the evidence of transition obtained from surface temperatures and shadowgraph pictures represents some average or most probable location of transition. It was found that at small to moderate angles of attack, a rough comparison could be made between the shadowgraph indication and that segment of the recovery-factor curve just aft of the peak value.<sup>4</sup> Thus, in figure 20 the location of transition is seen to move forward on the lee side and aft on the windward side with increasing angle of attack. At  $\alpha$  greater than  $10^\circ$  there is an apparent reversal of trend on the windward side, with transition (as defined herein) moving toward the nose.

---

<sup>4</sup>A similar comparison of temperature data and schlieren photographs in reference 14 showed agreement at the location of the peak temperature.

There remains the possibility that these transition data are being influenced by the flow expansion at the shoulder, in a manner similar to that described in reference 15. It was found therein that a strong flow expansion ( $58^\circ$  included angle cone-cylinder) resulted in the growth of a "new" laminar boundary layer behind the juncture. However, from examination of the present data it is apparent that the relatively weaker shoulder flow expansions of the present investigation were too weak to cause a similar behavior, although just a suggestion of this effect may be seen at  $\theta = 180^\circ$  in figure 9(c). Hence, although recovery temperatures in transition zones may have been slightly influenced by the flow expansion at the shoulder, it is believed that the location of the transition zone is not significantly altered and that the present results are representative of slender bodies.

Boundary-layer separation.- The circumferential location of boundary-layer separation as a function of angle of attack, shown in figure 21, is for flow conditions at the midpoint (lengthwise) of the cylindrical afterbody. Separation moved rapidly around the body as angle of attack was increased to about  $10^\circ$ . With further increase in angle of attack there was relatively little change. A rough correlation exists between the location of the separation line and certain features of the recovery-factor distributions shown in figure 12. At angles of attack above about  $15^\circ$  either a definite decrease in circumferential recovery-factor gradient or a minimum recovery-factor value is associated with the separation point. A tentative conclusion based on the china-clay studies is that the separated flow region, for  $\alpha$  from  $10^\circ$  to  $25^\circ$ , is by no means a "dead air" or low-velocity region. In fact, it appears from the drying patterns (e.g.,  $\alpha = 15^\circ$  in fig. 7) that the heat-transfer rate to the surface on the lee side of the model is of considerable magnitude.

It is also interesting to note that some of the variations observed in lee-side recovery factors (fig. 12) can be associated with the different separation flow patterns shown in figures 6 and 8. For angles of attack less than  $15^\circ$ , where the effect of boundary-layer transition on temperature distributions is relatively large, there is the flow visualized in figure 8(a) at an angle of attack of  $10^\circ$ . Here there is thickening of the boundary layer on the lee side with some separated flow that has not broken free of the surface. At  $\alpha = 15^\circ$ , where lee-side recovery factors have started to drop, there is the flow indicated in figure 8(b) where the vortices have broken free of the model but are still symmetrical, while at  $\alpha = 25^\circ$  (fig. 8(c)) the vortices have fallen into a vortex-street pattern. This last condition corresponds to the minimum recovery factor on the lee side of the model.<sup>5</sup> At  $\alpha = 35^\circ$ , where the temperature pattern is assuming

<sup>5</sup>One characteristic of the separation vortex pattern deserves mention. At  $\alpha = 25^\circ$  a certain flow instability, as a function of time, was observed to occur. The pattern of figure 8(c) was apparently a semisteady condition which was frequently interrupted by alternate shedding of vortices in what might be termed "bursts." Frequency or length of "burst" periods was not determined.



characteristics of transverse-cylinder flow, the vortex street disappears and, as shown in figure 8(d), is replaced by a dead air space followed by a turbulent wake.

### Recovery Factors Based on Local Conditions

Effect of angle of attack.- A representative variation of recovery factor based on local stream conditions with angle of attack and circumferential location is shown in figure 25. The data are based on the experimental Mach number distributions of figure 24 and are presented both as measured and as corrected for shell conduction error. Recovery factors on the free-stream basis are also shown for comparison. With increasing angle of attack the corrected local recovery factor decreases from about 0.86 at  $\alpha = 0^\circ$  to 0.81 at  $\alpha = 45^\circ$ , while free-stream recovery factor, in contrast, increases from 0.86 to 0.93 over the same interval. The variation of recovery factor with circumferential angle at  $\alpha = 25^\circ$  shows, as would be expected, that the substantial difference between  $\eta_{r,\infty}$  and  $\eta_{r,l}$  at  $\theta = 0^\circ$  is diminished as the flow is accelerated to about the free-stream Mach number at  $\theta = 90^\circ$ . Now, the reasons for the decrease of local recovery factor at high angles of attack are not clearly understood, although it has been suggested that a portion of the drop could be attributed to the effect of strong local pressure gradients. Indeed, to date, the results of several theoretical investigations indicate that such an effect could exist, and in at least one experimental investigation a small decrease of recovery factor was noted in the region of strong pressure gradients on a spherical nose (ref. 16). However, there remains the possibility that other factors may be contributing to the observed decrease.

Mach number effect.- A sizable decrease of surface temperature, in response to the change of local flow conditions at the shoulder of the cone, is illustrated in figures 10(e) and 16(b) for regions of laminar boundary-layer flow. It is believed that for the most part this decrease can be related to the change in local Mach number, for when recovery factors are evaluated on the local-stream basis (shown in fig. 16(b)), there is a good alinement of the data in the entire laminar flow region at lower free-stream Mach numbers and a sizable reduction in the recovery-factor decrement at the shoulder for  $M_\infty = 5.04$ . In the high Mach number range of these tests, however, the local-stream basis of evaluation appears to lose effectiveness, that is, it no longer accounts for the temperature drop at the shoulder. For example, the  $\eta_{r,\infty}$  decrement shown in figure 10(e) for  $M_\infty = 6.30$  at  $\alpha = 0^\circ$  can be reduced only from the indicated 0.018 to 0.014 when the temperature data are evaluated on the basis of local flow conditions. Although the reason for this change of behavior at high Mach numbers is not understood, a similar decrease of local recovery factor (although for a much blunter nose cone) has also been observed by Sternberg (ref. 15) at  $M_\infty = 3.02$  and 3.55. He concludes that the pressure drop at

the shoulder had a lasting effect on the subsequent boundary-layer development and that it is not sufficient to describe the boundary-layer properties (in this region) in terms of the local Mach number. Thus, although further investigation is necessary to fix the relationship between these two independent observations, it is indicated that under certain conditions a strong pressure gradient can, of itself, influence recovery temperatures.

Local recovery factors at zero angle of attack for the polished model surface are given as a function of local Mach number in figure 26. The experimental data are compared with the theoretical predictions of Polhausen ( $N_{Pr}^{1/2}$ ), Van Driest (ref. 17), and Young and Janssen (ref. 18) for laminar boundary-layer flow. The turbulent boundary-layer data are compared with the theories of Ackerman ( $N_{Pr}^{1/3}$ ), Van Driest (ref. 19), and Tucker and Maslen (ref. 20). The Prandtl numbers of the present investigation are referred to the surface temperature, since it is probable that the temperature of the air adjacent to the surface has a strong influence upon the magnitude of heat transfer within the boundary layer. (Note that Prandtl numbers decrease at Mach numbers greater than 4.5 as a result of the heated wind tunnel airstream.) The data presented are indicative of the range of recovery factors at each test Mach number; intermediate values are omitted for the sake of clarity.

The laminar-boundary-layer data do not agree over the entire Mach number range with any of the theoretical curves although comparison is perhaps most favorable with the  $N_{Pr,e}^{1/2}$  prediction. This is not surprising since model surface temperatures are relatively low. It is of greater significance, however, to compare with the theories of Van Driest and of Young and Janssen, since each of these may also be applied to the prediction of recovery factors for actual flight conditions where surface temperatures are much higher and the  $N_{Pr,e}^{1/2}$  prediction may not be valid. It can be seen that both of these theories give about the same agreement in the Mach number range of this investigation. The comparison is good at Mach numbers up to 4, with an overestimate of about 1 percent in the higher speed range. It might be well to mention, in passing, that a significant decrease of flight recovery factor with Mach number is indicated in reference 18, while, in contrast, a much smaller decrease is shown in reference 17. Eckert (ref. 21) has shown that this difference is, for the most part, due to the definition of stagnation temperature in reference 18. In reference 18, the stagnation temperature used is that for a constant specific heat (equal to the free-stream value) and, since a variable specific heat was used in computing the insulated-surface temperature, it is readily seen that the resultant recovery factor will decrease considerably at high flight speeds. If either a variable or average specific heat is used throughout (e.g., ref. 21) the recovery-factor predictions of reference 18 would not differ appreciably from those of reference 17.

In the turbulent case the  $N_{Pr,e}^{1/3}$  prediction appears to be an upper boundary for recovery factors representative of fully developed turbulent flow, while maximum transition values lie above. The modified Tucker-Maslen theory<sup>6</sup> agrees favorably at lower Mach numbers but is about 1 percent low in the higher speed range. The turbulent theory of Van Driest, which in its present development is applicable to both wind-tunnel and flight conditions at Mach numbers up to about 4, does not compare as favorably with the experimental data.

### CONCLUSIONS

Experimental temperature recovery factors were determined on a slender cone-cylinder model at Mach numbers up to 6.30 and Reynolds numbers from  $1.8 \times 10^6$  to  $11.0 \times 10^6$  per foot. The angle-of-attack range was  $0^\circ$  to  $45^\circ$  at Mach numbers less than 3.50,  $0^\circ$  to  $25^\circ$  at Mach number 4.23, and  $0^\circ$  to  $15^\circ$  at Mach numbers from 5.04 to 6.30. The following conclusions have been drawn from the results of this investigation:

1. Temperature recovery factors at angles of attack up to  $10^\circ$  vary in a complex manner, apparently in response to changes in the location and extent of the boundary-layer transition region.
2. At angles of attack above  $10^\circ$ , windward-side recovery factors (free-stream basis) gradually rise as a result of adiabatic compression to above 0.95 at an angle of attack of  $45^\circ$ , a value some 6 percent above the zero-angle case. Lee-side recovery factors decrease, as a result of flow separation, to minimum values in the angle-of-attack range from  $25^\circ$  to  $35^\circ$ . At  $M_\infty = 3.02$  the minimum was 0.83, about 7 percent below the corresponding zero-angle value.
3. At angles of attack greater than about  $25^\circ$ , a circumferential recovery-temperature pattern similar to that for a transverse cylinder is developed on the cylindrical afterbody.
4. In the high Reynolds number (low Mach number) range of the present investigation, the average free-stream recovery factor for the entire surface does not exceed the value for zero angle of attack by more than 1 percent for angles of attack up to  $35^\circ$ .
5. When based on local flow conditions, recovery factors on the windward meridian gradually decrease with increasing angle of attack (except

---

<sup>6</sup>Modified after the manner suggested in reference 22, where the arithmetic mean temperature of the boundary layer was used to define a

Prandtl number in the equation  $\eta_{r,l} = N_{Pr} \left( \frac{N+1+0.528 M_l^2}{3N+1+M_l^2} \right)$

---

for the interval between  $0^\circ$  and  $5^\circ$ ), dropping at  $M_\infty = 3.50$ , from 0.86 at zero angle of attack to 0.81 at an angle of attack of  $45^\circ$  on the cone.

6. At zero angle of attack, recovery factors (local flow basis) for laminar boundary-layer flow are in agreement with  $N_{Pr,e}^{1/2}$  (Prandtl number based on wall temperature), while the Van Driest or Young and Janssen predictions overestimate by about 1 percent at Mach numbers greater than 4. For turbulent flow  $N_{Pr,e}^{1/3}$  establishes an upper limit for recovery factors based on local conditions while the modified Tucker-Maslen theory is about 1 percent low at higher Mach numbers.

7. For the range of conditions in this investigation there is no significant variation of recovery factor with either Reynolds number or Mach number in regions of either laminar or turbulent boundary-layer flow. However, the effect of Reynolds number on transition location is a determining factor in lee-side surface temperature levels.

Ames Aeronautical Laboratory  
National Advisory Committee for Aeronautics  
Moffett Field, Calif., July 20, 1955

#### REFERENCES

1. Gazley, C., and Adams, P.: Temperature Recovery Factors on a Body of Revolution at Mach Numbers of 1.79 and 4.50. Rep. R52A0509, General Electric Co., Guided Missiles Department, Aug. 1952.
2. Jack, John R., and Moskowitz, Barry: Experimental Investigation of Temperature Recovery Factors on a  $10^\circ$  Cone at Angle of Attack at a Mach Number of 3.12. NACA TN 3256, 1954.
3. Eggers, A. J., Jr., and Nothwang, George J.: The Ames 10- by 14-Inch Supersonic Wind Tunnel. NACA TN 3095, 1954.
4. Allen, H. Julian, and Perkins, Edward W.: Characteristics of Flow Over Inclined Bodies of Revolution. NACA RM A50L07, 1951.
5. Gazley, Carl, Jr.: The Use of the China-Clay Lacquer Technique for Detecting Boundary-Layer Transition. Rep. R49A0536, General Electric Co., General Engineering and Consulting Lab., Mar. 1950.
6. Goldstein, David L., and Scherrer, Richard: Design and Calibration of a Total-Temperature Probe for Use at Supersonic Speeds. NACA TN 1885, 1949.

~~CONFIDENTIAL~~

7. Walter, L. W., and Lange, A. H.: Surface Temperature and Pressure Distributions on a Circular Cylinder in Supersonic Cross-Flow. NAVORD Rep. 2854, Naval Ordnance Lab., June 5, 1953.
8. Savin, Raymond C.: Application of the Generalized Shock-Expansion Method to Inclined Bodies of Revolution Traveling at High Supersonic Airspeeds. NACA TN 3349, 1955.
9. Staff of the Computing Section, Center of Analysis, under the direction of Zdenek Kopal: Tables of Supersonic Flow Around Yawing Cones. M.I.T. Dept. of Electrical Eng., Center of Analysis, Tech. Rep. No. 1, Cambridge, 1947.
10. Staff of the Computing Section, Center of Analysis, under the direction of Zdenek Kopal: Tables of Supersonic Flow Around Yawing Cones. M.I.T. Dept. of Electrical Eng., Center of Analysis, Tech. Rep. No. 3, Cambridge, 1947.
11. Staff of the Computing Section, Center of Analysis, under the direction of Zdenek Kopal: Tables of Supersonic Flow Around Cones of Large Yaw. M.I.T. Dept. of Electrical Eng., Center of Analysis, Tech. Rep. No. 5, Cambridge, 1949.
12. Roberts, Richard C., and Riley, James D.: A Guide to the Use of the M.I.T. Cone Tables. NAVORD Rep. 2606, Naval Ordnance Lab., Apr. 1, 1953.
13. Emmons, H. W.: The Laminar-Turbulent Transition in a Boundary Layer, Part I. Jour. Aero. Sci., vol. 18, no. 7, July 1951, pp. 490-498.
14. Brinich, Paul F.: Boundary-Layer Transition at Mach 3.12 With and Without Single Roughness Elements. NACA TN 3267, 1954.
15. Sternberg, Joseph: The Transition from a Turbulent to a Laminar Boundary Layer. BRL Rep. No. 906, Ballistic Research Labs., Aberdeen Proving Ground, May 1954.
16. Stine, Howard A., and Wanlass, Kent: Theoretical and Experimental Investigation of Aerodynamic-Heating and Isothermal Heat-Transfer Parameters on a Hemispherical Nose With Laminar Boundary Layer at Supersonic Mach Numbers. NACA TN 3344, 1954.
17. Van Driest, E. R.: The Laminar Boundary Layer with Variable Fluid Properties. Rep. AL-1866, North American Aviation, Inc., Jan. 19, 1954.
18. Young, George B. W., and Janssen, Earl: The Compressible Boundary Layer. Jour. Aero. Sci., vol. 19, no. 4, Apr. 1952, pp. 229-236, and 288.

19. Van Driest, E. R.: The Turbulent Boundary Layer with Variable Prandtl Number. Rep. AL-1914, North American Aviation, Inc., Apr. 2, 1954.
20. Tucker, Maurice, and Maslen, Stephen H.: Turbulent Boundary-Layer Temperature Recovery Factors in Two-Dimensional Supersonic Flow. NACA TN 2296, 1951.
21. Eckert, Ernst R. G.: Survey on Heat Transfer at High Speeds. Tech. Rep. 54-70, Wright Air Development Center, Apr. 1954.
22. Stine, Howard A., and Scherrer, Richard: Experimental Investigation of the Turbulent-Boundary-Layer Temperature-Recovery Factor on Bodies of Revolution at Mach Numbers from 2.0 to 3.8. NACA TN 2664, 1952.
23. The NBS-NACA Tables of Thermal Properties of Gases. Table 2.44, Prandtl Number of Dry Air, Compiled by Joseph Hilsenrath, National Bureau of Standards, U.S. Department of Commerce, 1950.

~~CONFIDENTIAL~~

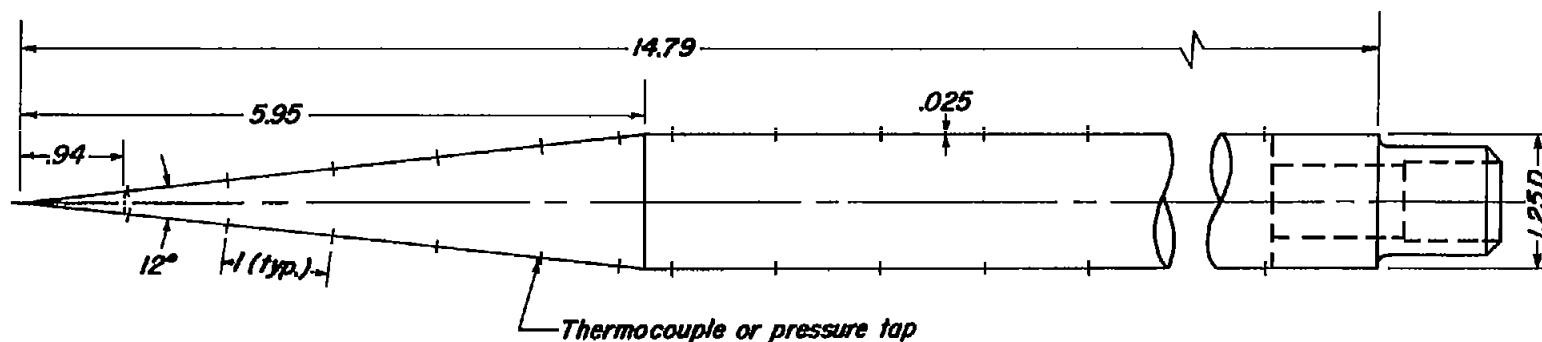
TABLE I.- TEST CONDITIONS, TEMPERATURE MODELS

Angle of attack, deg	Meridian angle, deg	Free-stream Mach number								
		3.02	3.50		4.23		5.04		6.30	
		Free-stream Reynolds number per ft/10 <sup>6</sup>								
		8.6	11.3	8.6	4.2	8.6	4.2	4.2	1.8	1.8
0	0,90,180,270	x	x	x	x	x	x	x	x	x
1	0,180	x	x			x		x		x
2	0,180	x	x			x		x		x
4	0,180	x	x			x		x		x
5	0,45,90,135,180,270	x	x			x		x		x
10	0,45,90,135,180,270	x	x	x	x	x	x	x	x	x
15	0,45,90,135,180,270	x	x			x		x		x
25	0,45,90,135,180,270	x	x	x		x				
35	0,45,90,135,180,270	x	x							
45	0,45,90,135,180,270	x	x							
90		x								

TABLE II.- TEST CONDITIONS, PRESSURE MODEL

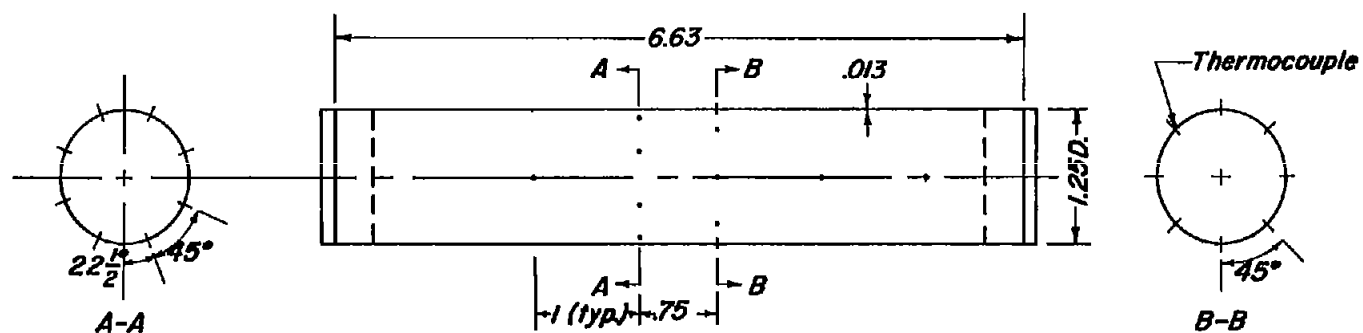
Angle of attack, deg	Meridian angle, deg	Free-stream Mach number								
		3.02	3.50		4.23		5.04		6.30	
		Free-stream Reynolds number per ft/10 <sup>6</sup>								
		8.6	11.3	8.6	4.2	8.6	4.2	4.2	1.8	1.8
0	0,180	x	x	x	x	x	x	x	x	x
1	0,180	x	x			x		x		
2	0,180	x	x			x		x		
4	0,180	x	x			x		x		
5	0,180	x	x			x		x		x
	45,90,135,270	x	x			x		x		
10	0,180	x	x	x	x	x	x	x	x	x
	45,135	x	x	x		x	x	x		x
	90,270	x	x	x		x	x	x	x	x
15	0,180	x	x			x		x		x
	45,90,135,270	x	x			x		x		
25	0,180	x	x	x		x				
	45,90,135,270	x	x							
35	0,180	x	x							

~~CONFIDENTIAL~~



(a) Cone-cylinder

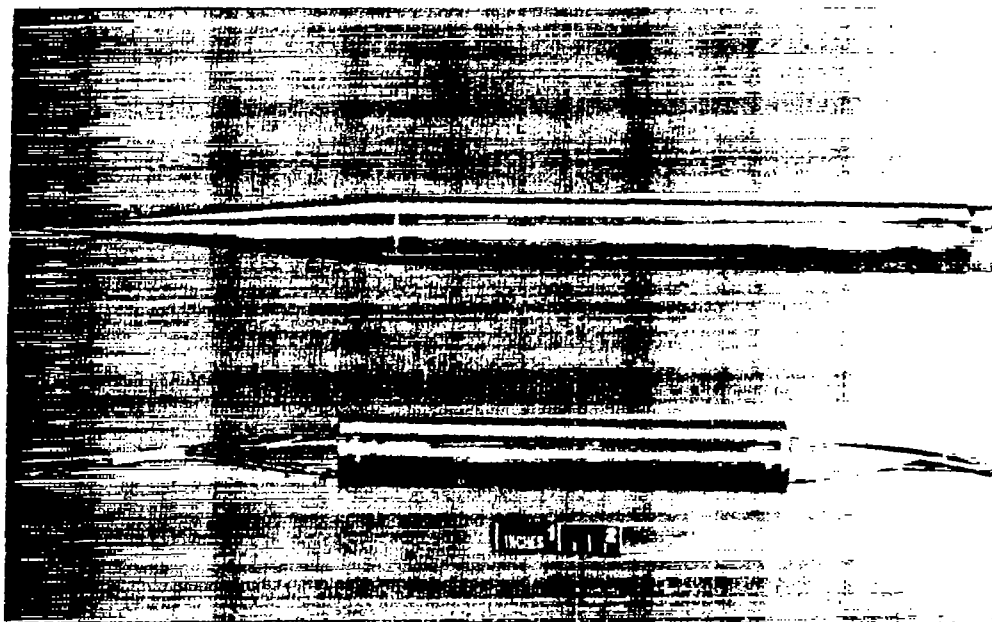
Note: All dimensions in inches.



(b) Crossflow cylinder

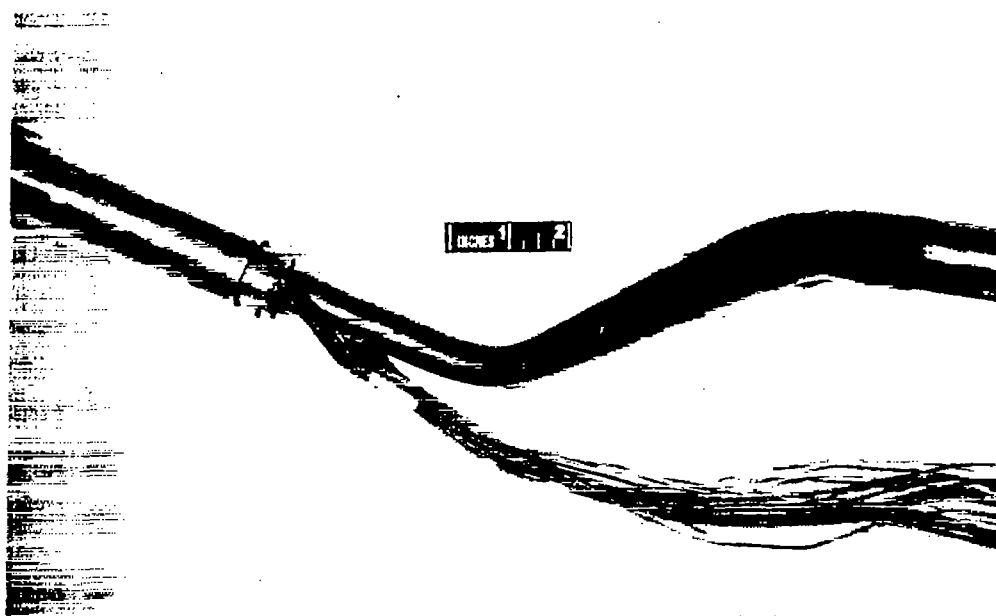
Figure 1.— Thermocouple and pressure tap-locations on test bodies.





A-19147.1

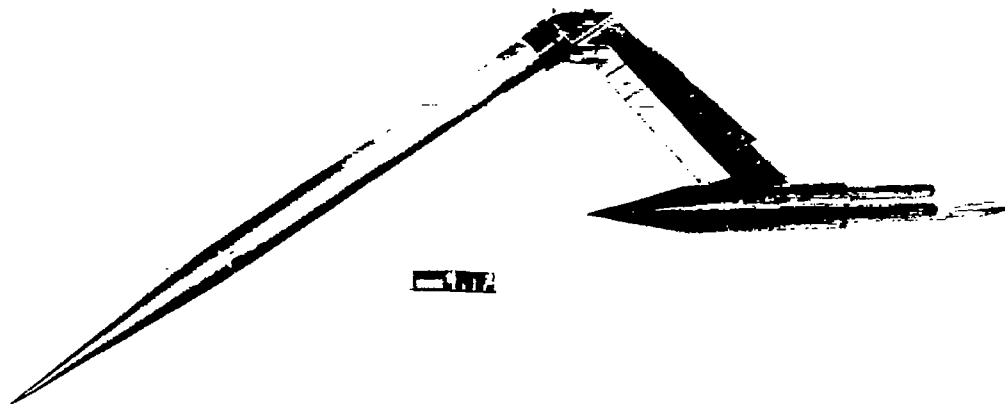
Figure 2.- Photograph of cone-cylinder and crossflow cylinder models.



A-19148

(a) Cone-cylinder on  $\alpha = 15^\circ$  support.

Figure 3.- Model support assemblies.



A-19149.1

(b) Cone-cylinder on  $\alpha = 35^\circ$  support.



A-19625

(c) Crossflow cylinder on fork support.

Figure 3.- Concluded.

CONFIDENTIAL

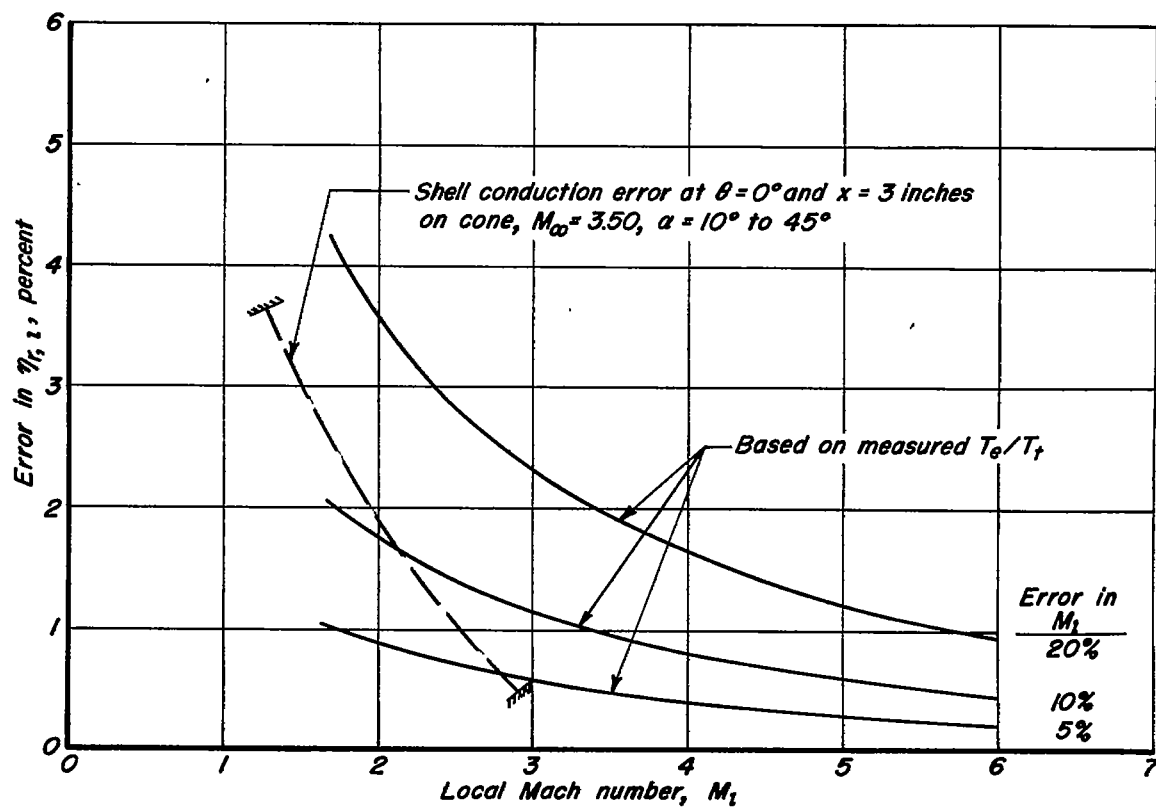
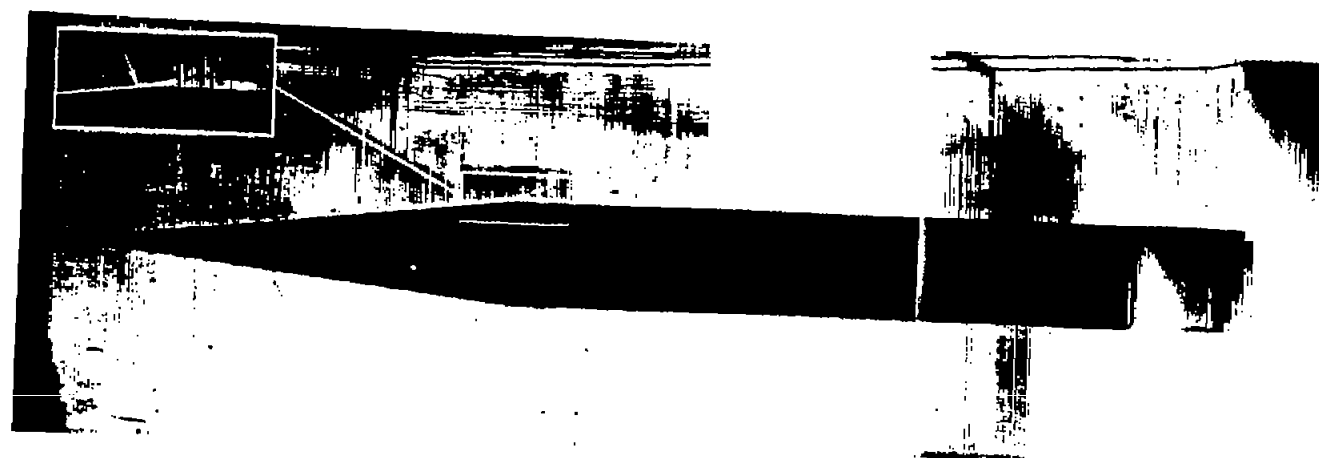
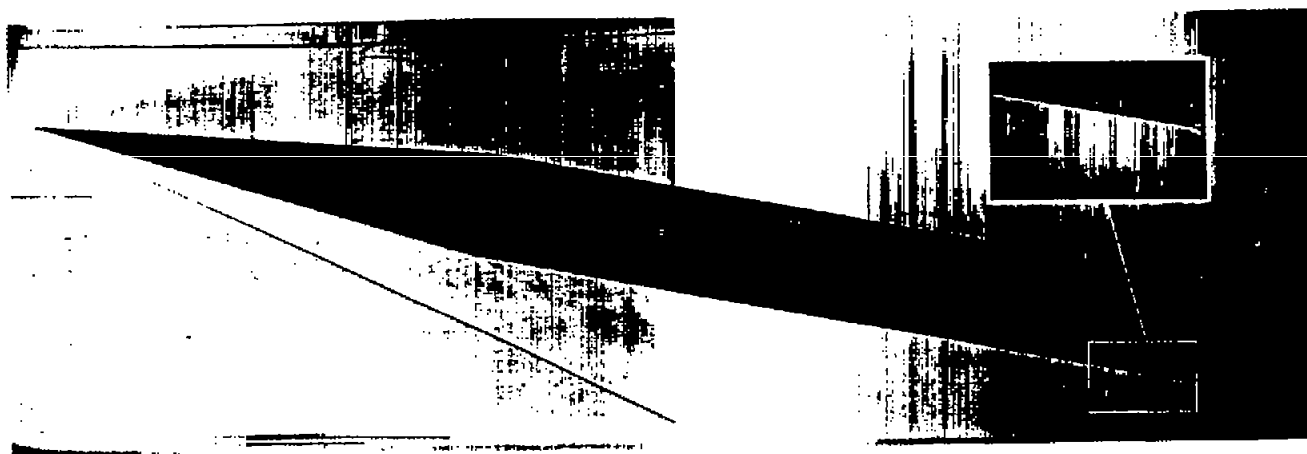


Figure 4.— Error in local temperature recovery factor resulting from either shell conduction or error in local Mach number.

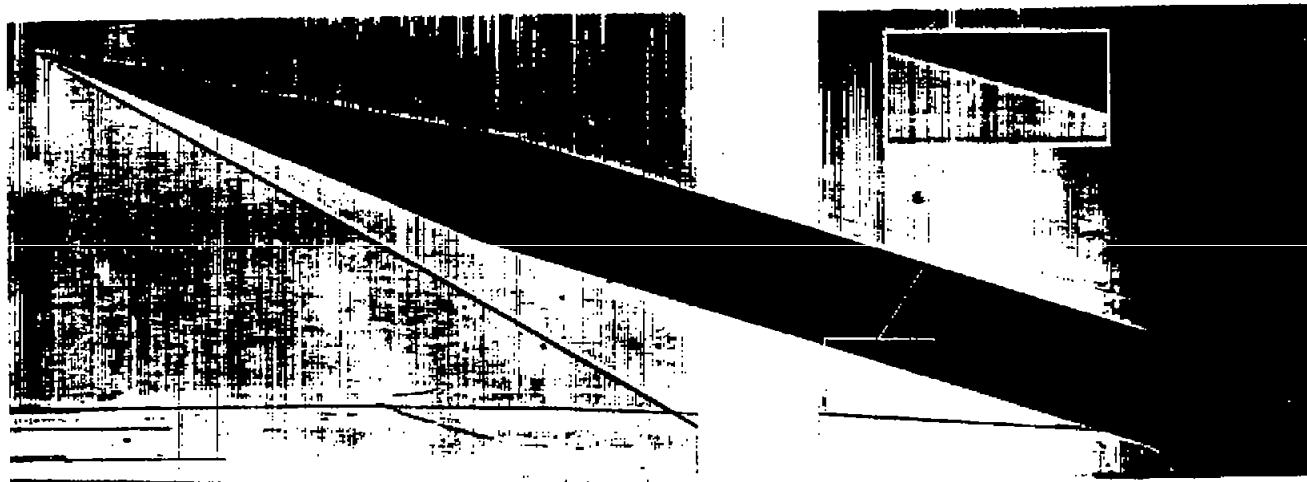
(a)  $\alpha = 0^\circ$ (b)  $\alpha = 5^\circ$ 

A-20004.2

Figure 5.- Shadowgraph pictures of cone-cylinder model showing location of boundary-layer transition;  $M_\infty = 3.02$ ,  $R = 8.6 \times 10^6$  per foot.



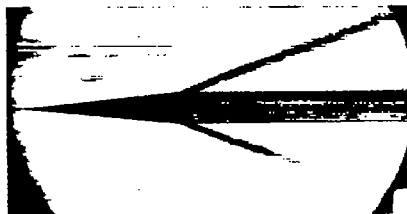
(c)  $\alpha = 10^\circ$



(d)  $\alpha = 15^\circ$

A-20004.1

Figure 5.- Concluded.

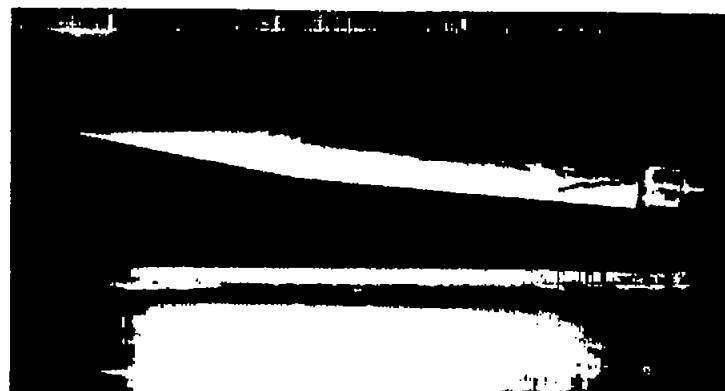
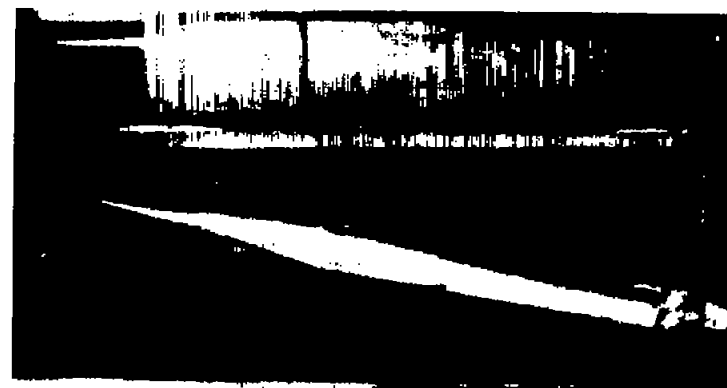
Plane of  $\theta = 0^\circ$  and  $180^\circ$ Plane of  $\theta = 90^\circ$  and  $270^\circ$  $\alpha = 5^\circ$  $\alpha = 10^\circ$  $\alpha = 15^\circ$  $\alpha = 25^\circ$ 

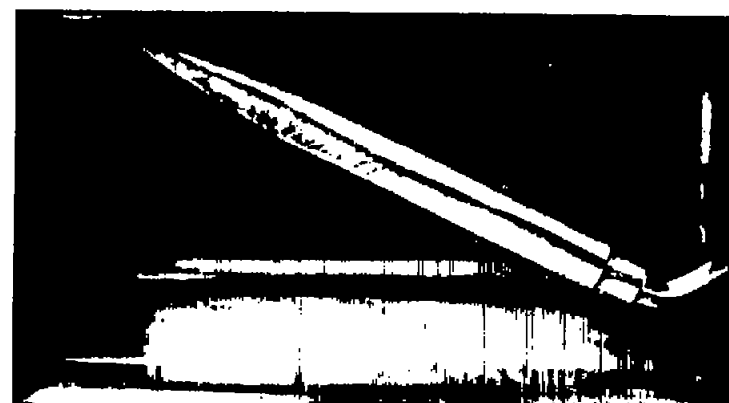
A-20002

 $\alpha = 35^\circ$ 

Figure 6.- Schlieren photographs of cone-cylinder model;  $M_\infty = 3.02$ ,  
 $R = 8.6 \times 10^6$  per foot.

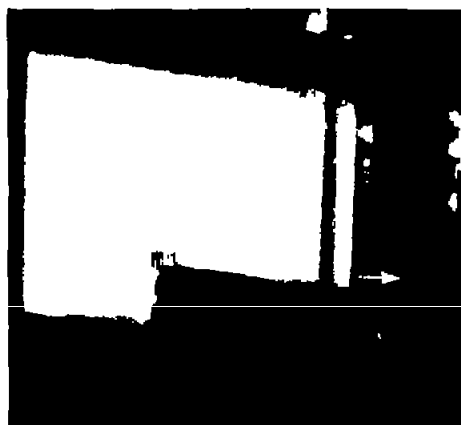
CONFIDENTIAL


 $\alpha = 5^\circ$ 

 $\alpha = 10^\circ$ 

 $\alpha = 15^\circ$ 

 $\alpha = 25^\circ$ 

A-20006

Figure 7.- Flow separation visualized by china-clay method;  $M_\infty = 3.02$ ,  $R = 8.6 \times 10^6$  per foot.

(a)  $M_{\infty} = 3.02$ ,  $\alpha = 10^{\circ}$ (b)  $M_{\infty} = 3.02$ ,  $\alpha = 15^{\circ}$ 

A-20007.1

(c)  $M_{\infty} = 3.02$ ,  $\alpha = 25^{\circ}$ (d)  $M_{\infty} = 3.02$ ,  $\alpha = 35^{\circ}$ 

Figure 8.- Vapor screen photographs of flow at approximately the midpoint of the afterbody of the cone-cylinder model at angles of attack from  $10^{\circ}$  to  $35^{\circ}$ ; flow direction indicated by arrows.



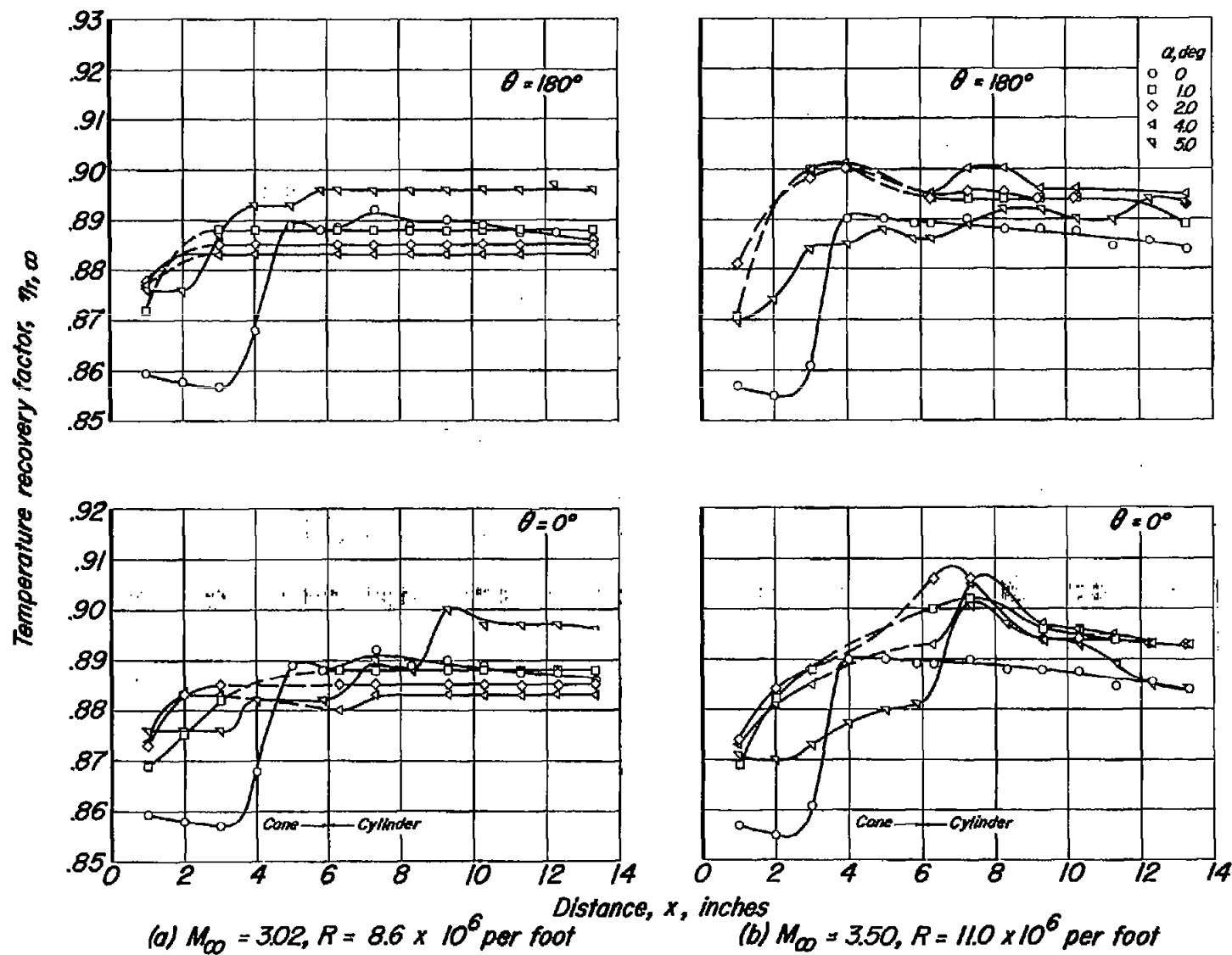


Figure 9.— Variation of recovery factor with distance along model at small angles of attack.

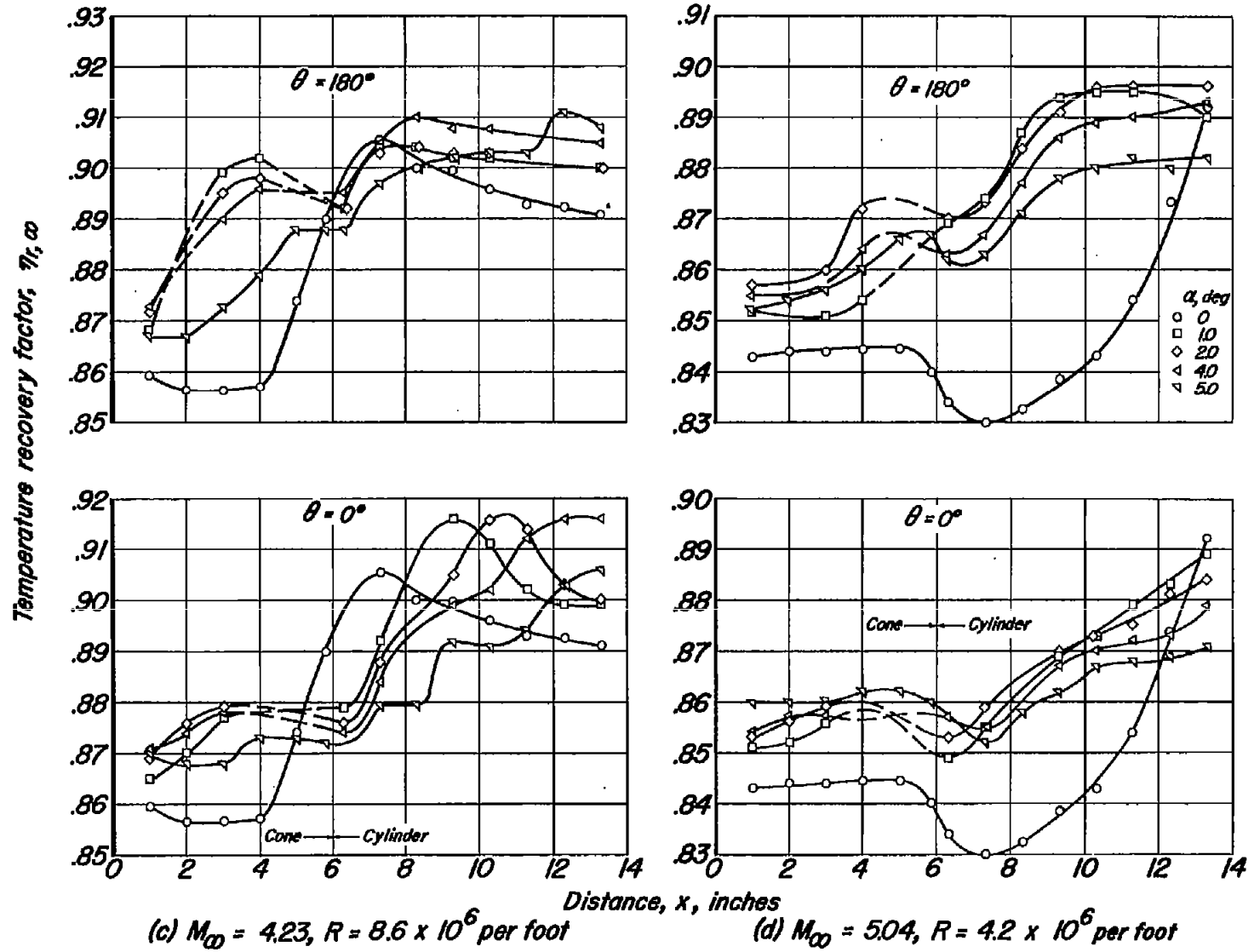
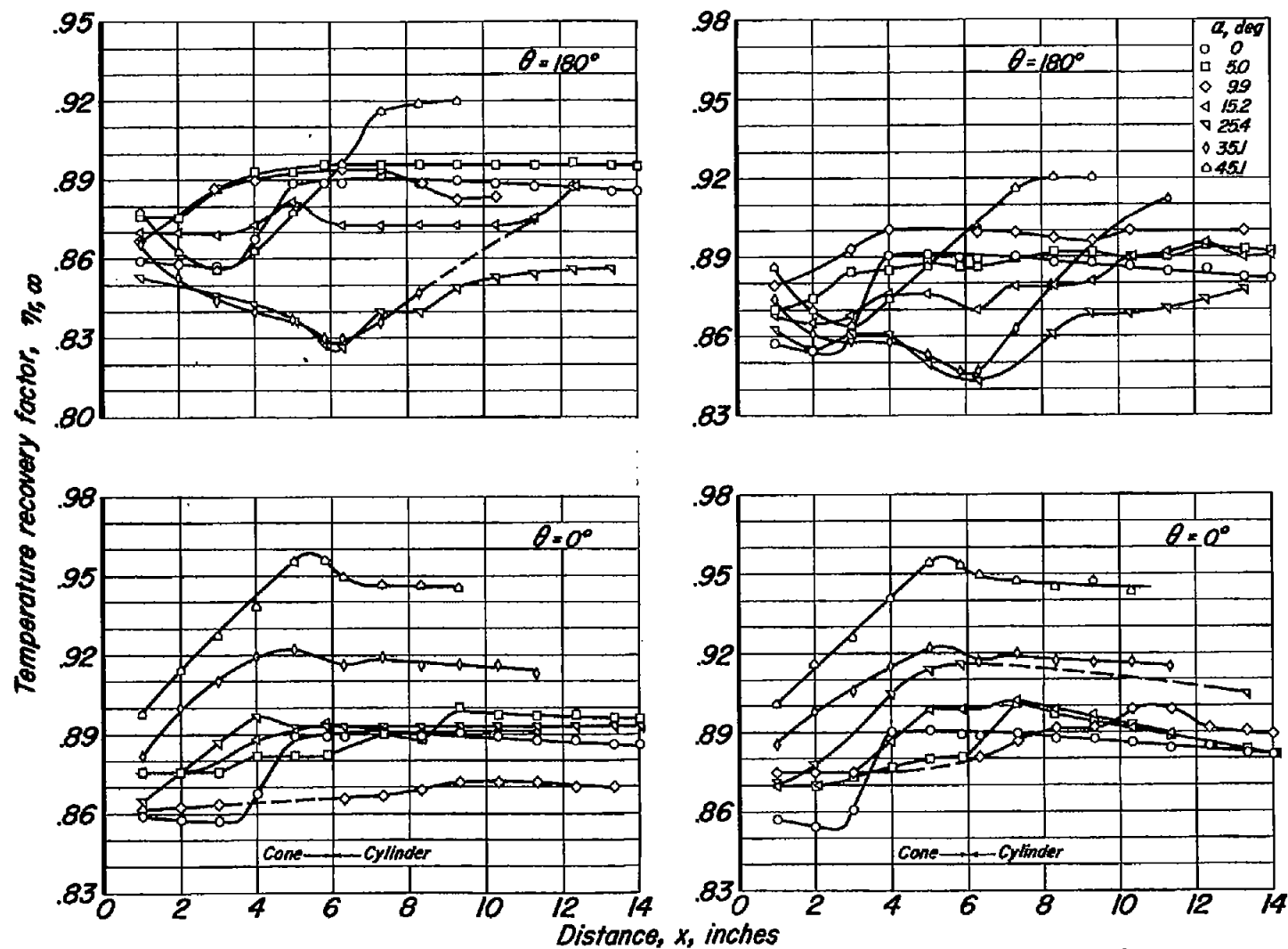


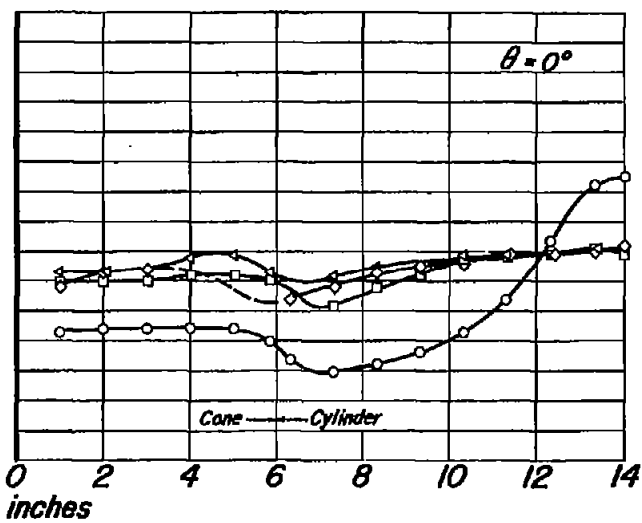
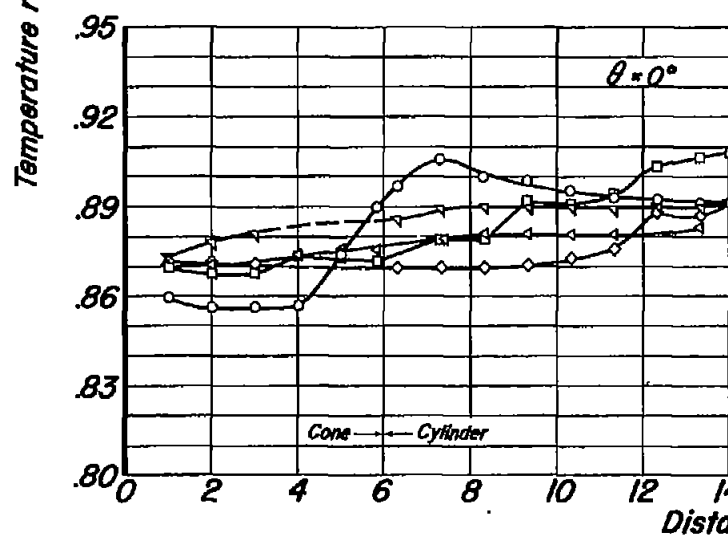
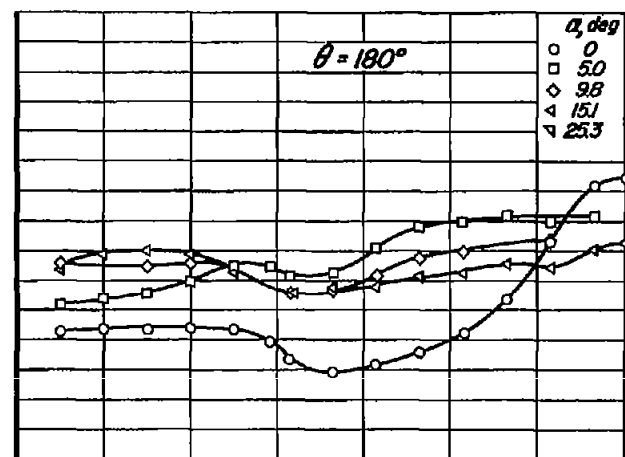
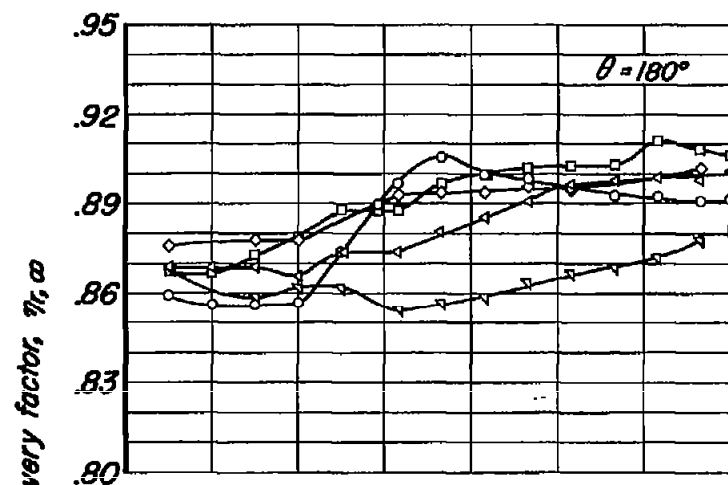
Figure 9.- Concluded.



(a)  $M_\infty = 3.02$ ,  $R = 8.6 \times 10^6$  per foot

(b)  $M_\infty = 3.50$ ,  $R = 11.0 \times 10^6$  per foot

Figure 10.—Variation of recovery factor with distance along model for several angles of attack.

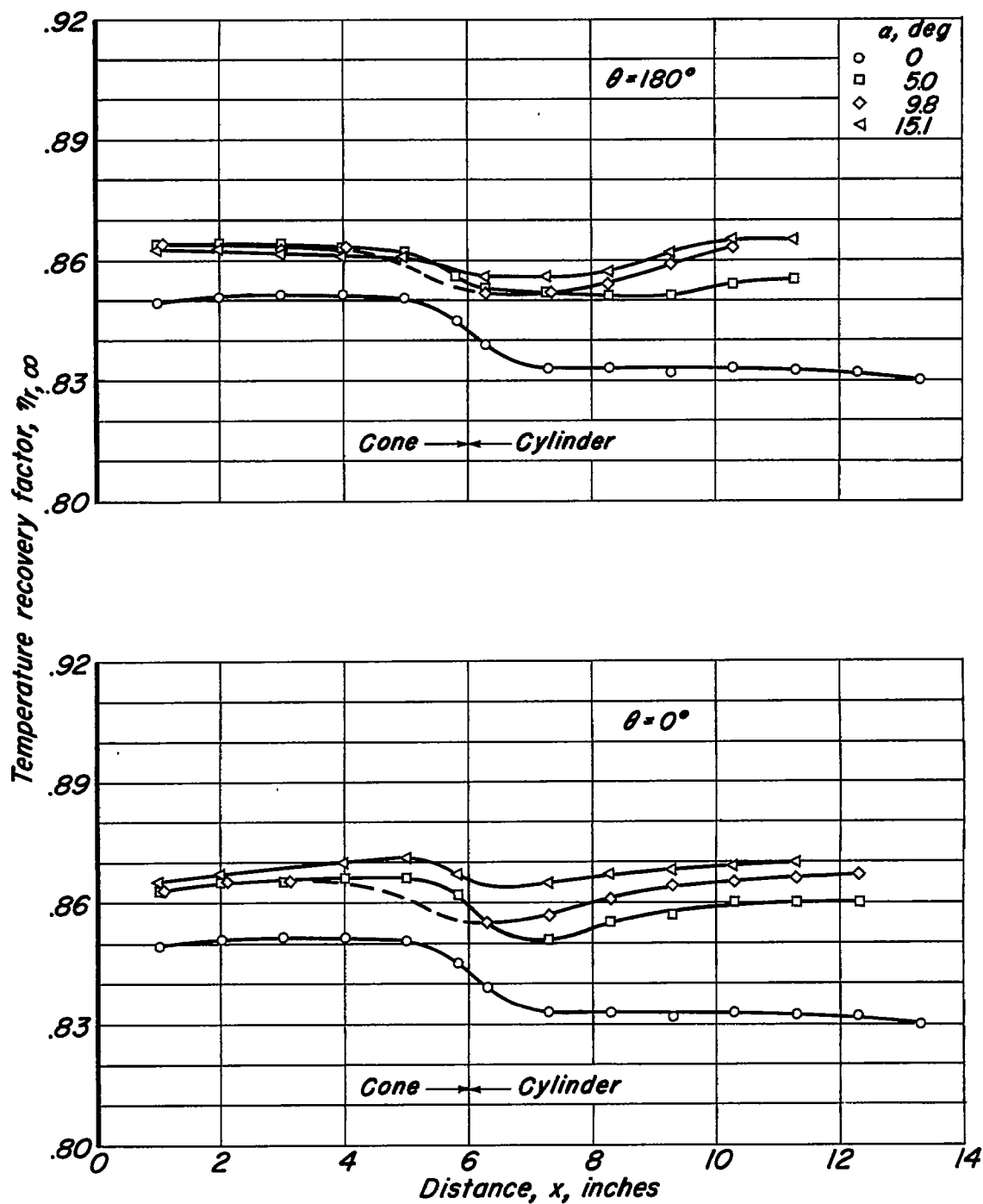


(c)  $M_\infty = 4.23$ ,  $R = 8.6 \times 10^6$  per foot

(d)  $M_\infty = 5.04$ ,  $R = 4.2 \times 10^6$  per foot

Figure 10.- Continued.

CONFIDENTIAL

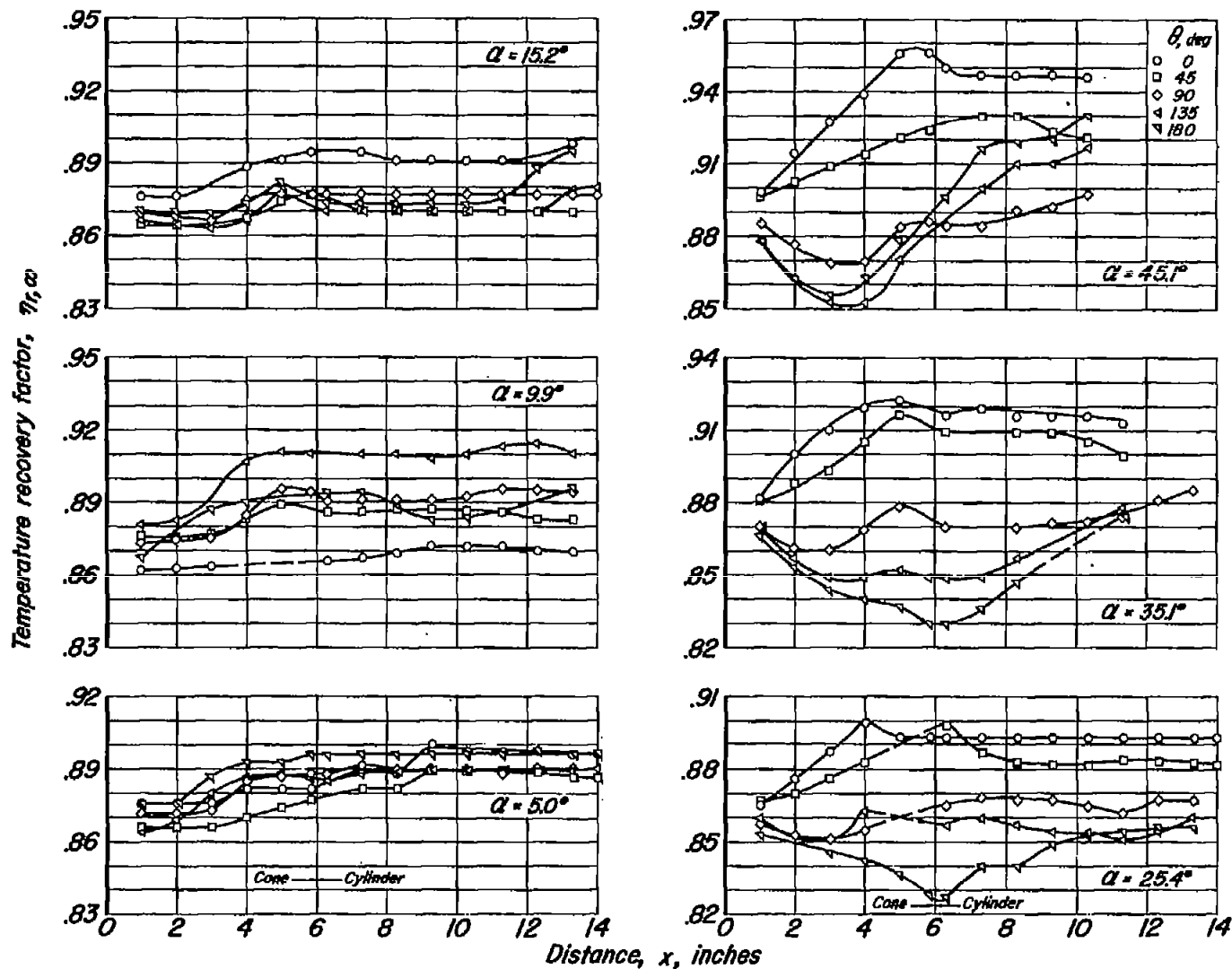


(e)  $M_\infty = 6.30$ ,  $R = 1.8 \times 10^6$  per foot

Figure 10.— Concluded.

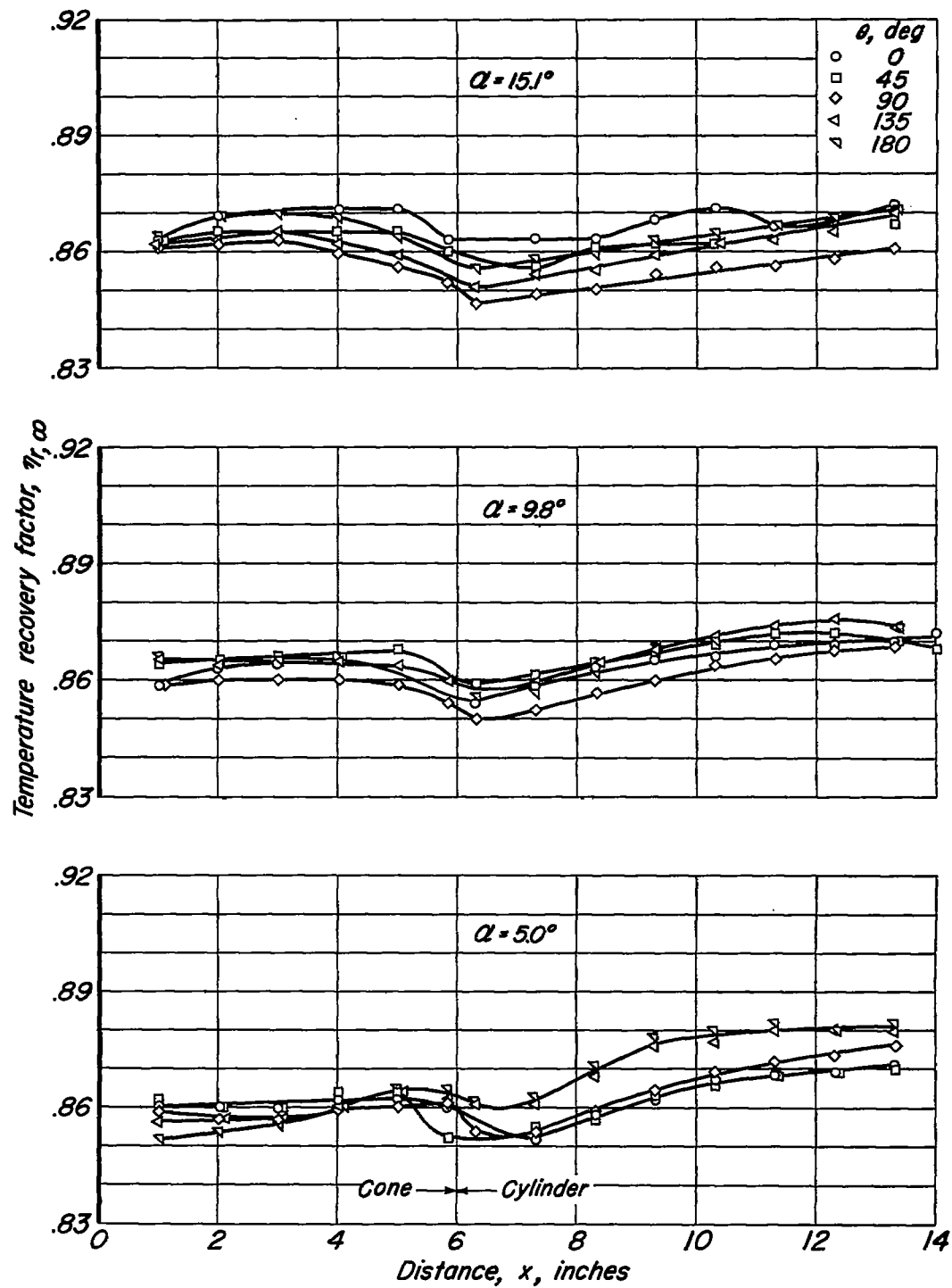
CONFIDENTIAL

CONFIDENTIAL



(a)  $M_\infty = 3.02$ ,  $R = 8.6 \times 10^6$  per foot

Figure 11.- Variation of recovery factor with distance along model on several meridian lines.



(b)  $M_\infty = 5.04$ ,  $R = 4.2 \times 10^6$  per foot

Figure 11.- Concluded.

CONFIDENTIAL

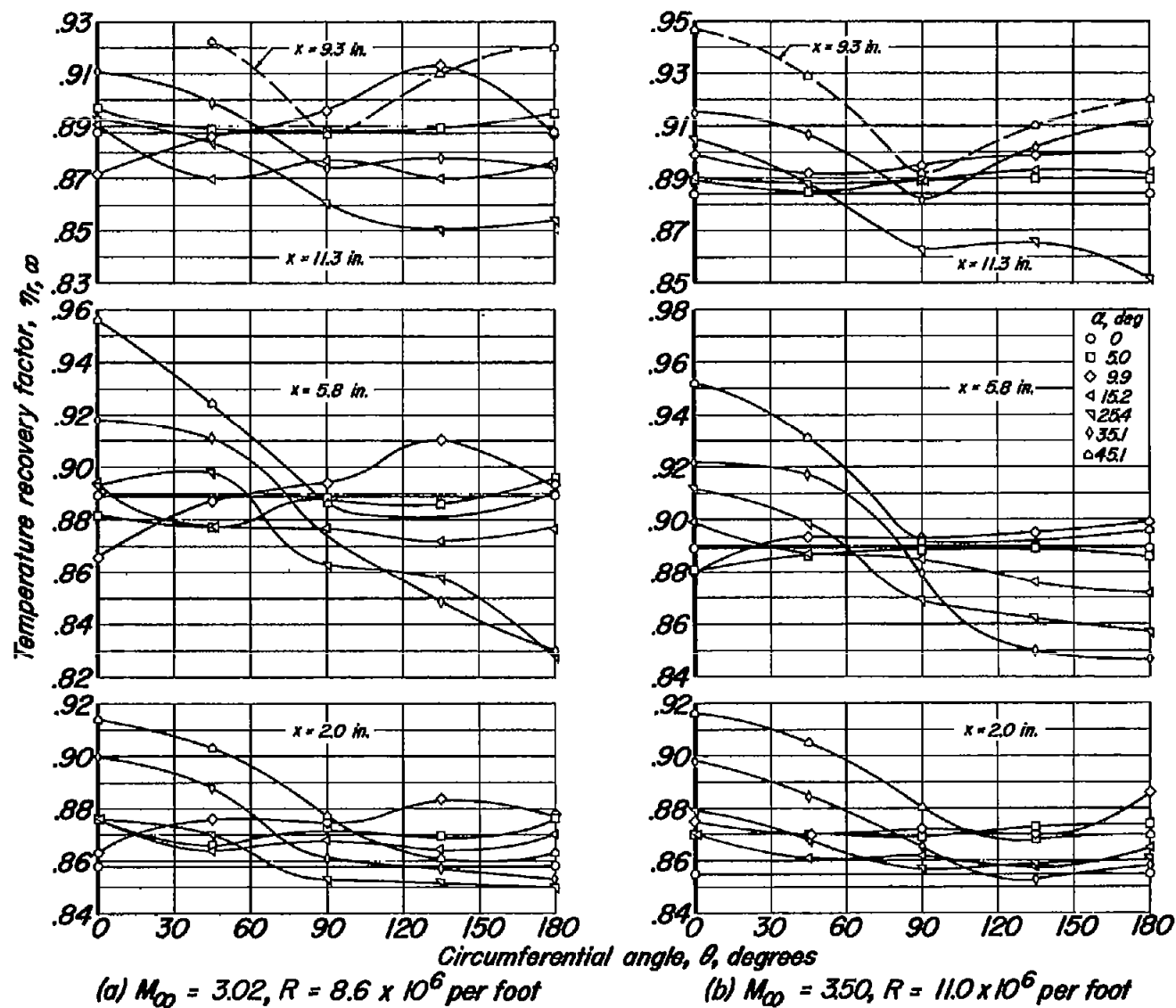
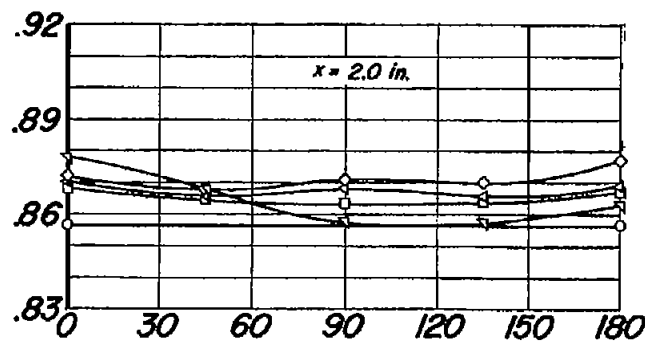
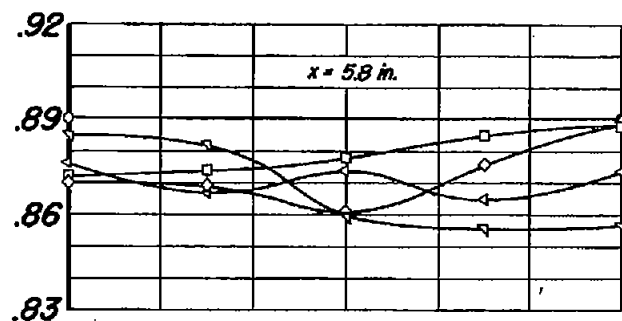
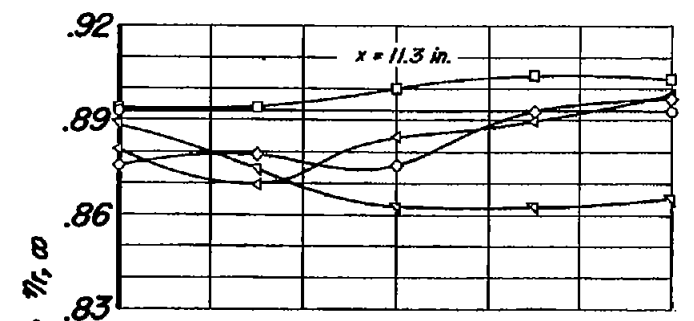
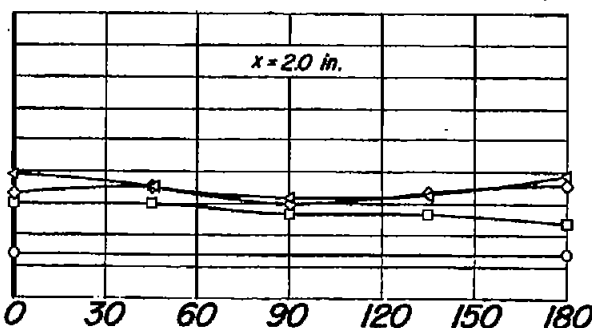
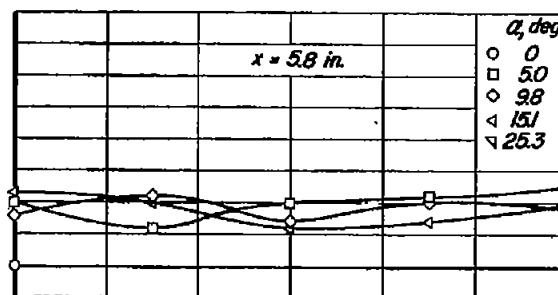
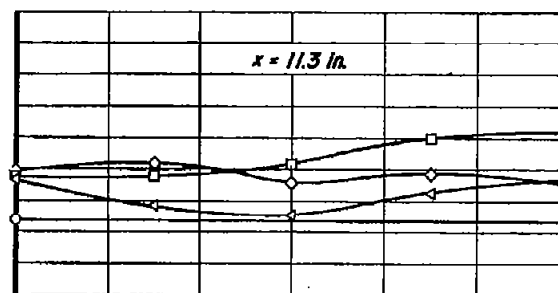


Figure 12.- Variation of recovery factor with circumferential location for several angles of attack.





(c)  $M_{\infty} = 4.23$ ,  $R = 8.6 \times 10^6$  per foot



(d)  $M_{\infty} = 5.04$ ,  $R = 4.2 \times 10^6$  per foot

Figure 12.- Continued.

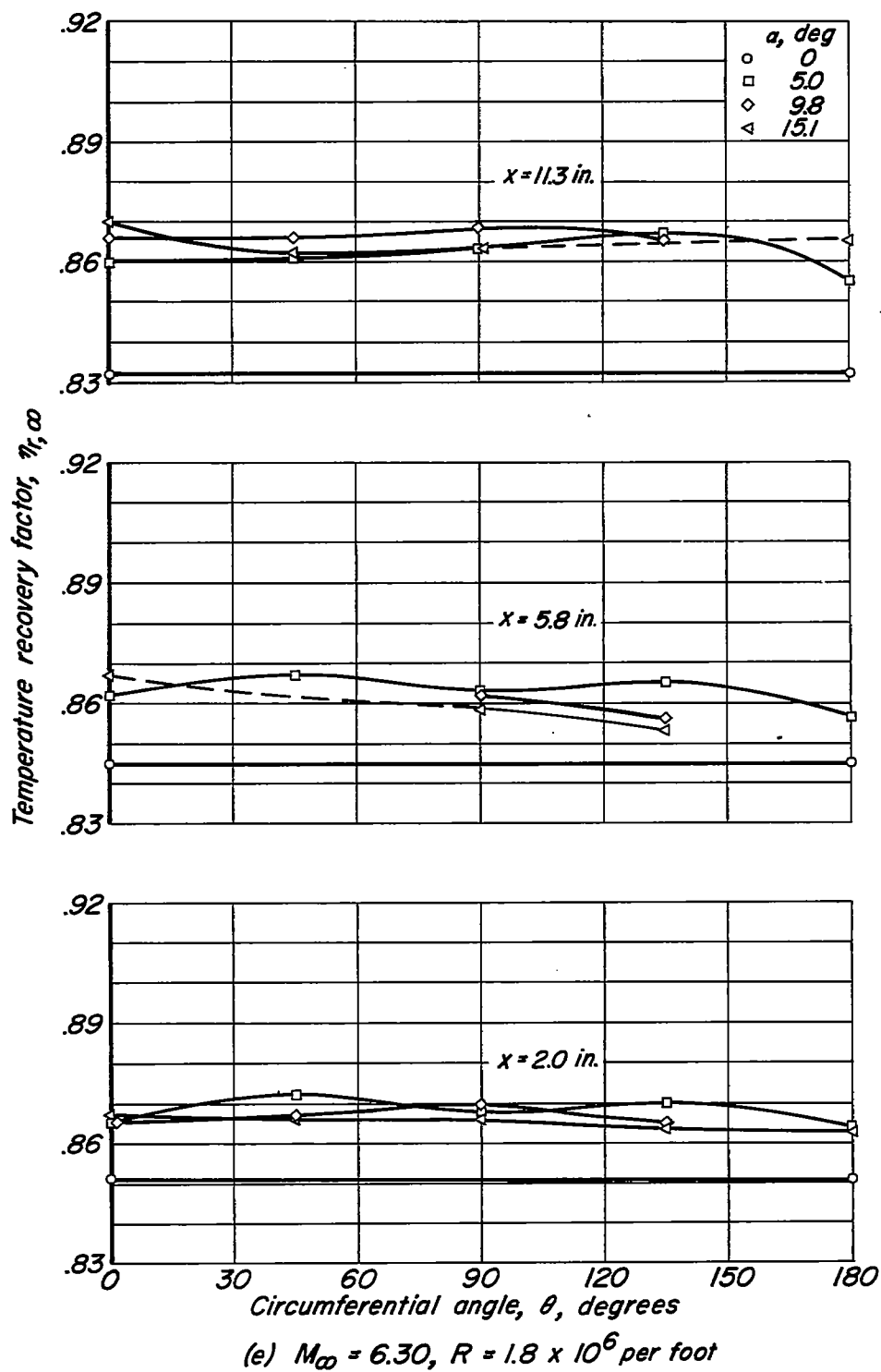


Figure 12.- Concluded.

CONFIDENTIAL

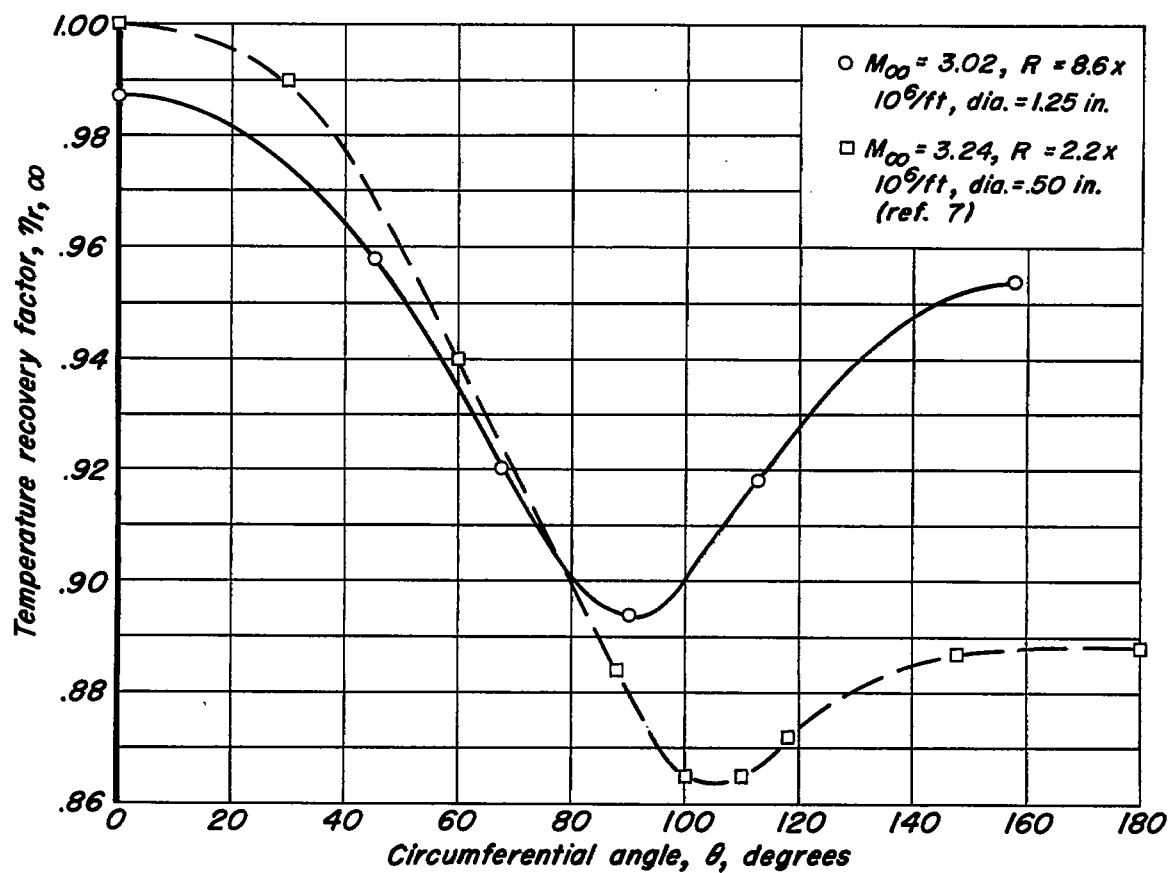


Figure 13.- Recovery-factor distribution on transverse cylinder.

CONFIDENTIAL

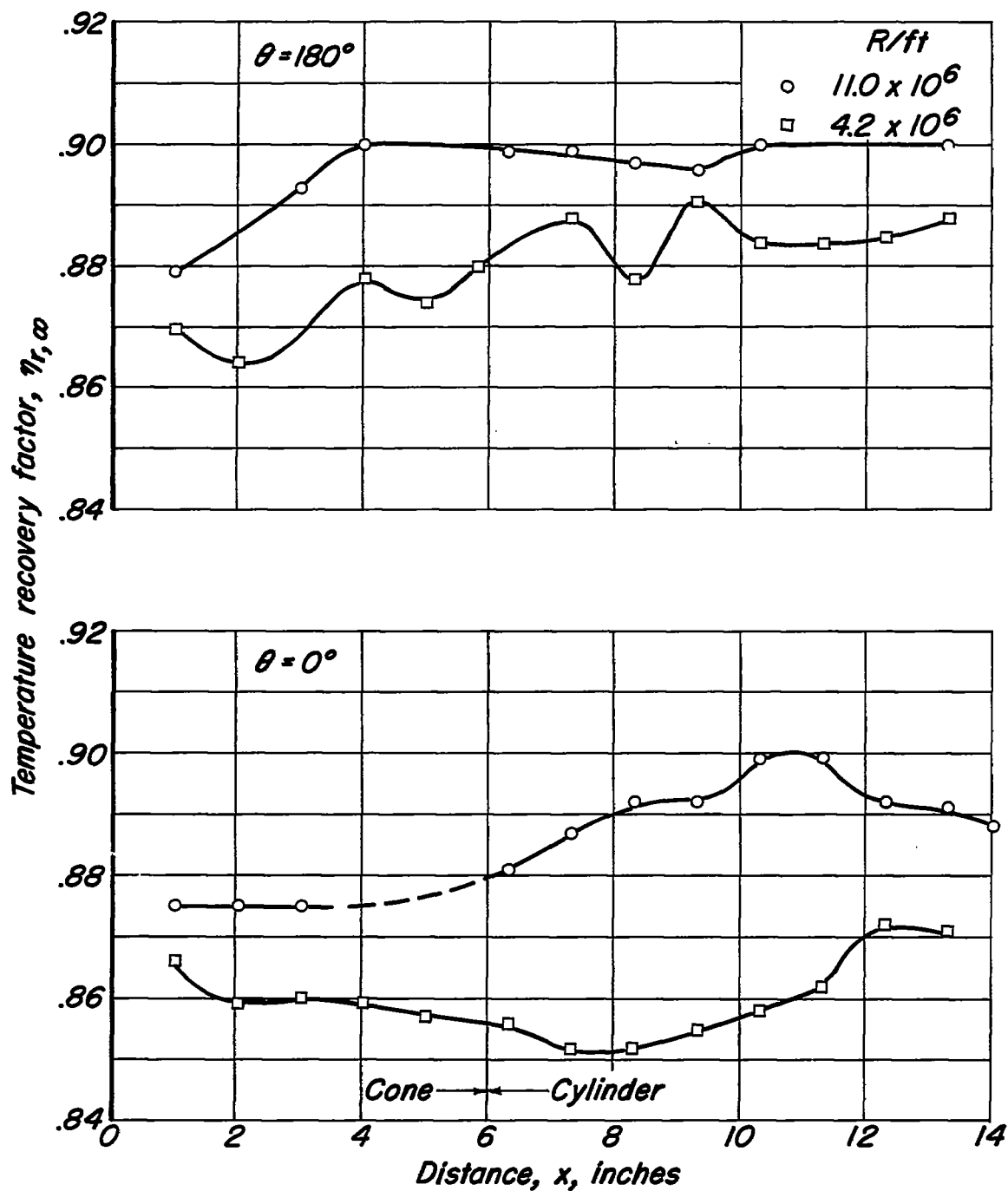
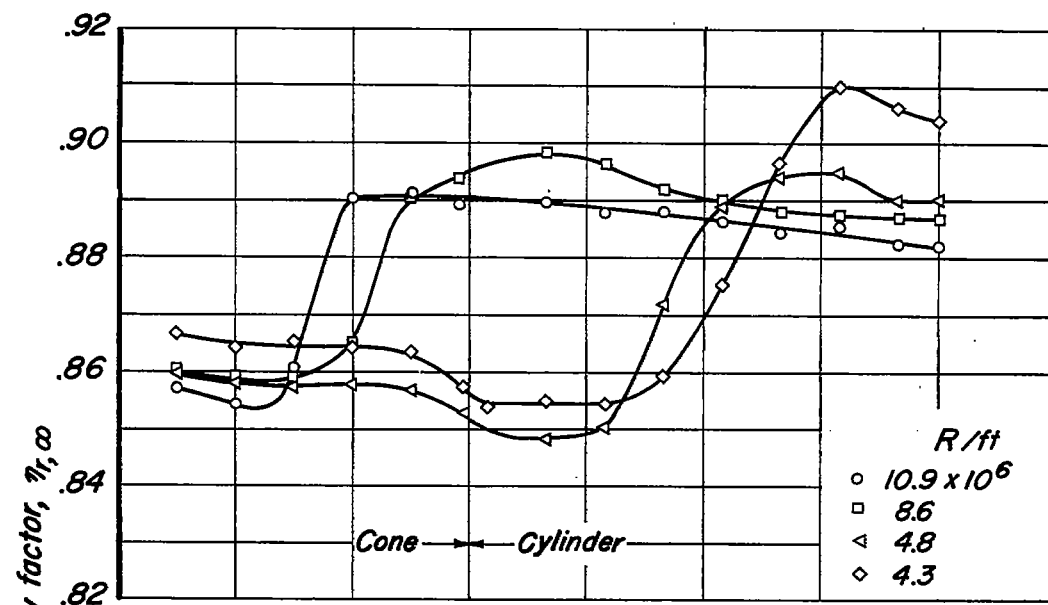
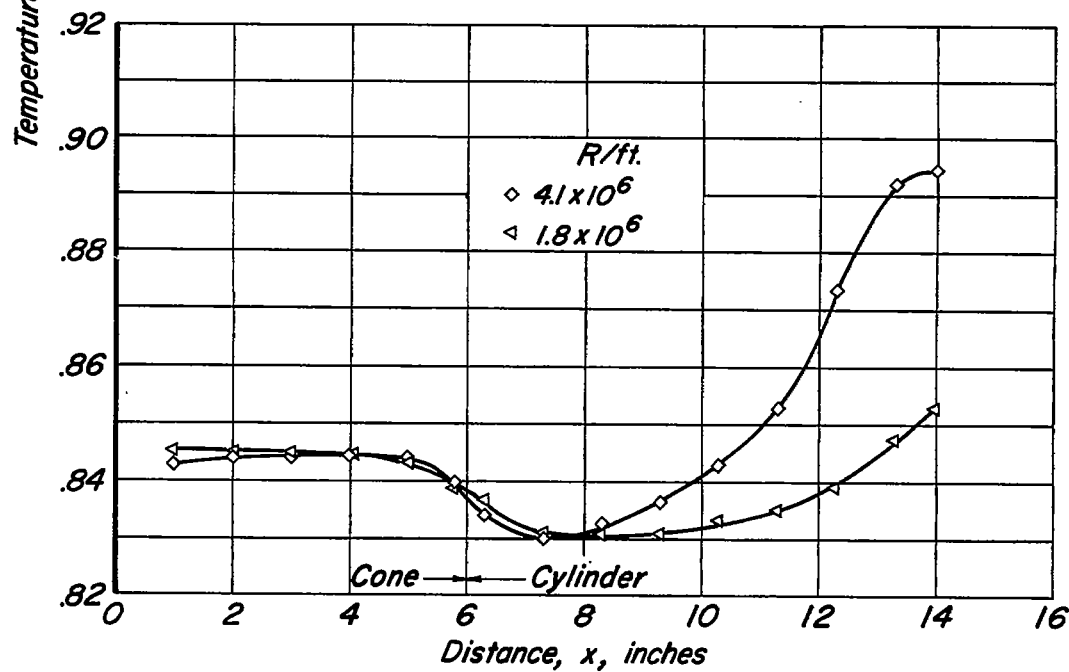


Figure 14.- Effect of Reynolds number on measured recovery factor at  $\alpha = 10^\circ$ ;  $M_\infty = 3.50$ .

(a)  $M_\infty = 3.50$ (b)  $M_\infty = 5.04$ Figure 15.- Effect of Reynolds number on measured recovery factor at  $\alpha = 0^\circ$

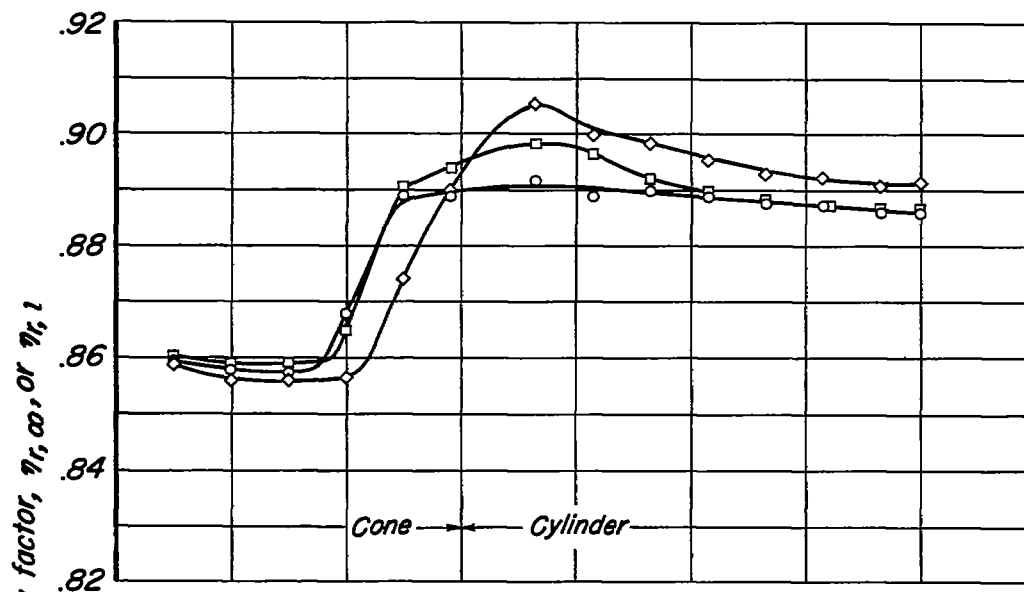
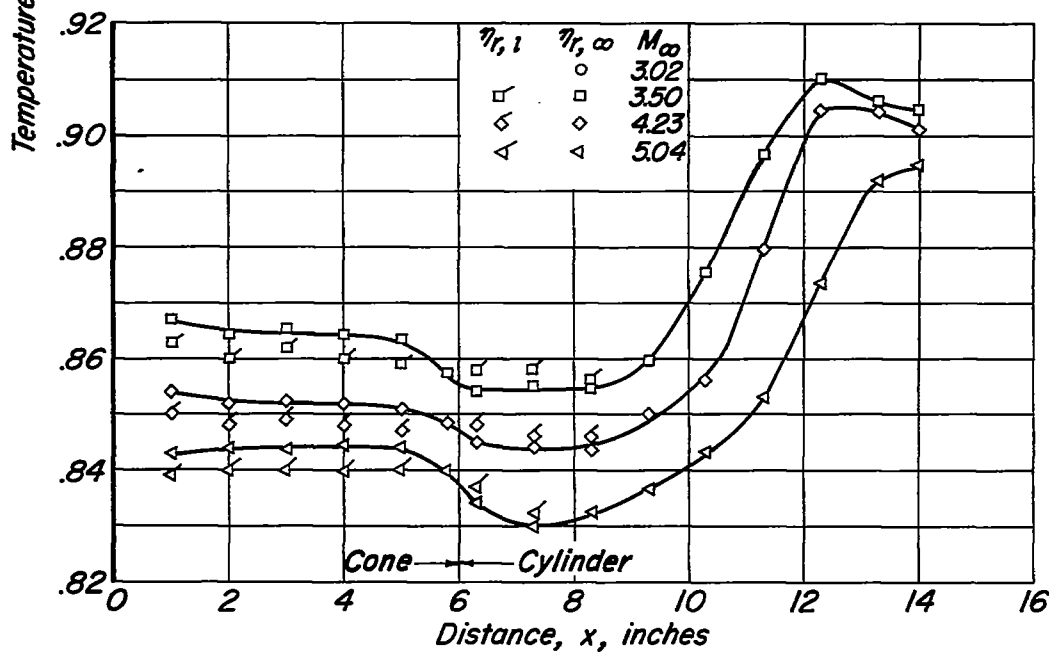
(a)  $R = 8.6 \times 10^6$  per foot(b)  $R = 4.2 \times 10^6$  per foot

Figure 16.- Variation of recovery factor with distance along model for several Mach numbers,  $R$  constant,  $\alpha = 0^\circ$

CONFIDENTIAL

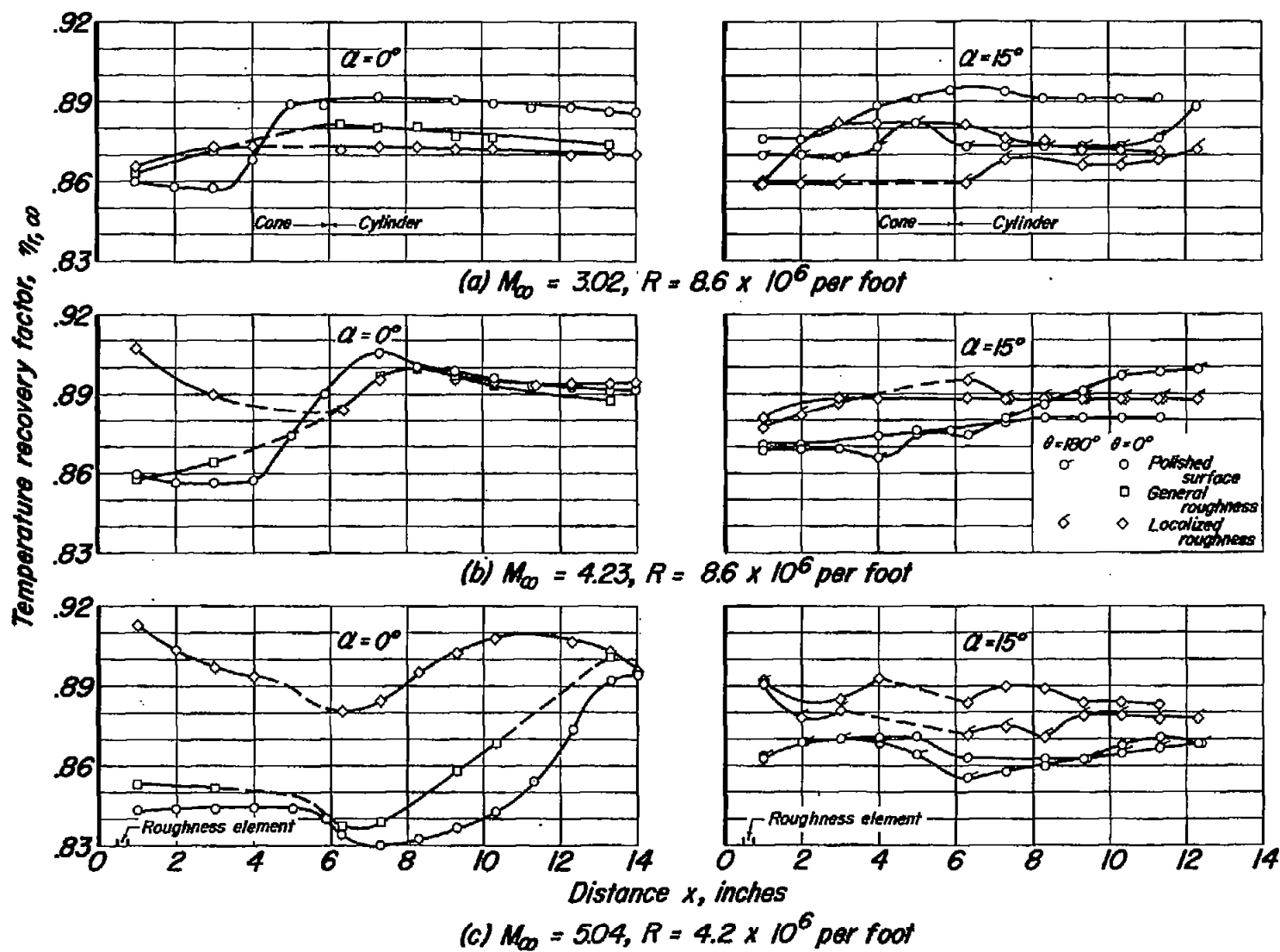
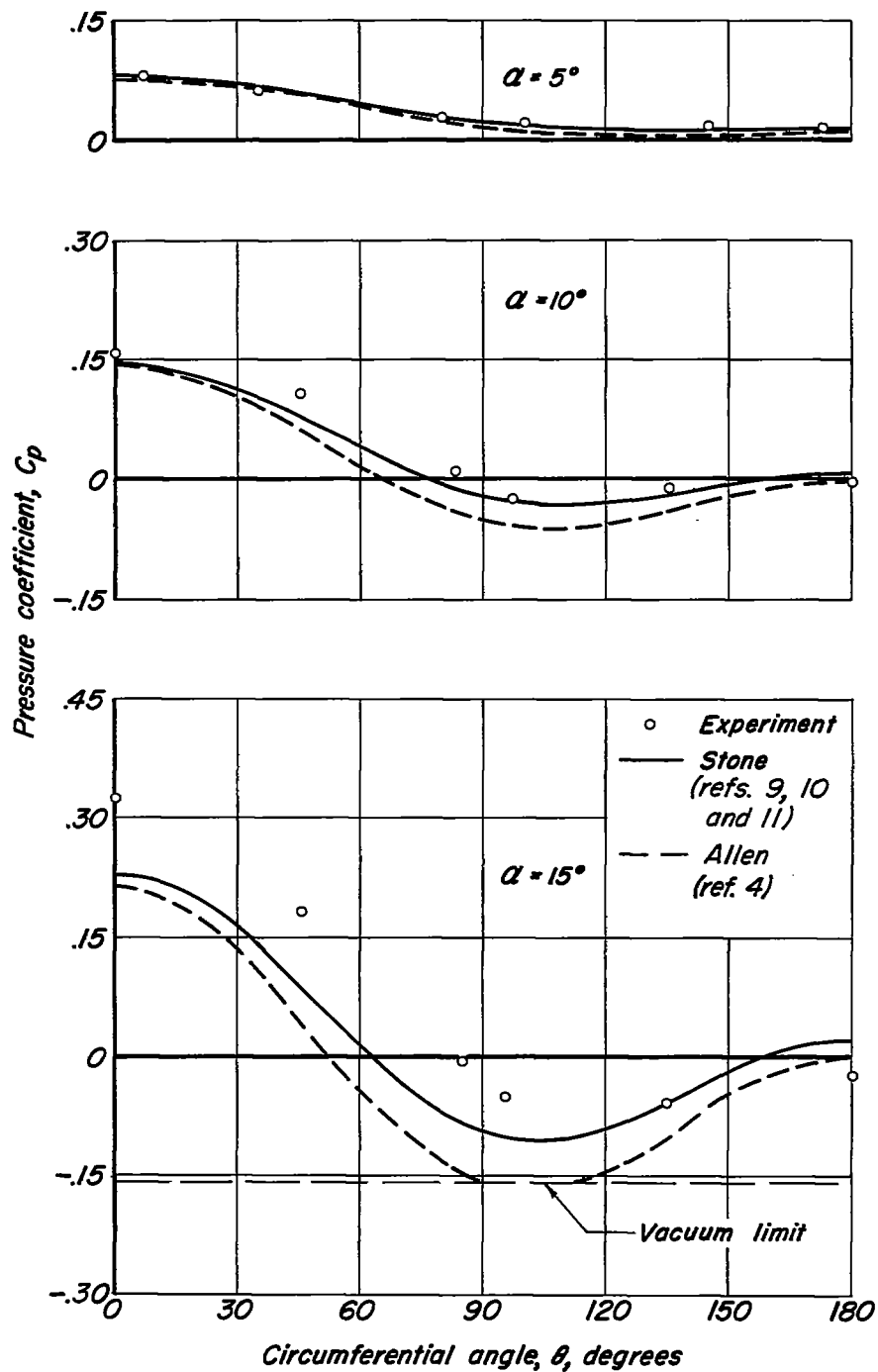


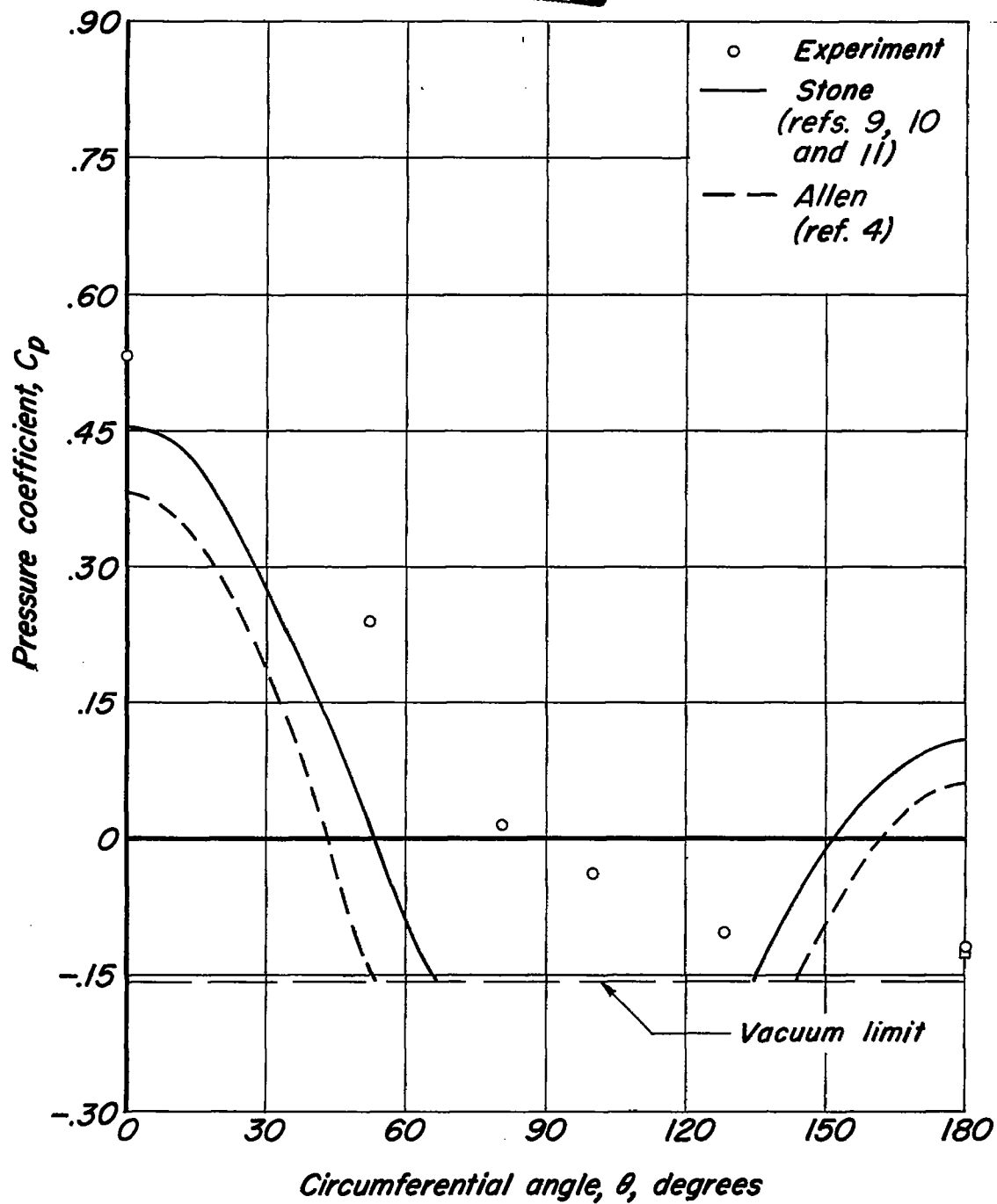
Figure 17.— Effect of surface roughness on recovery factor at  $\alpha = 0^\circ$  and  $\alpha = 15^\circ$ .



(a)  $\alpha = 5^\circ, 10^\circ$  and  $15^\circ$

Figure 18.— Circumferential pressure distributions at midpoint of conical nose at  $M_\infty = 3.02$ ,  $R = 8.6 \times 10^6$  per foot, and angles of attack to  $25^\circ$ ; comparison of theory and experiment.



~~CONFIDENTIAL~~

(b)  $\alpha = 25^\circ$

Figure 18.- Concluded.

~~CONFIDENTIAL~~

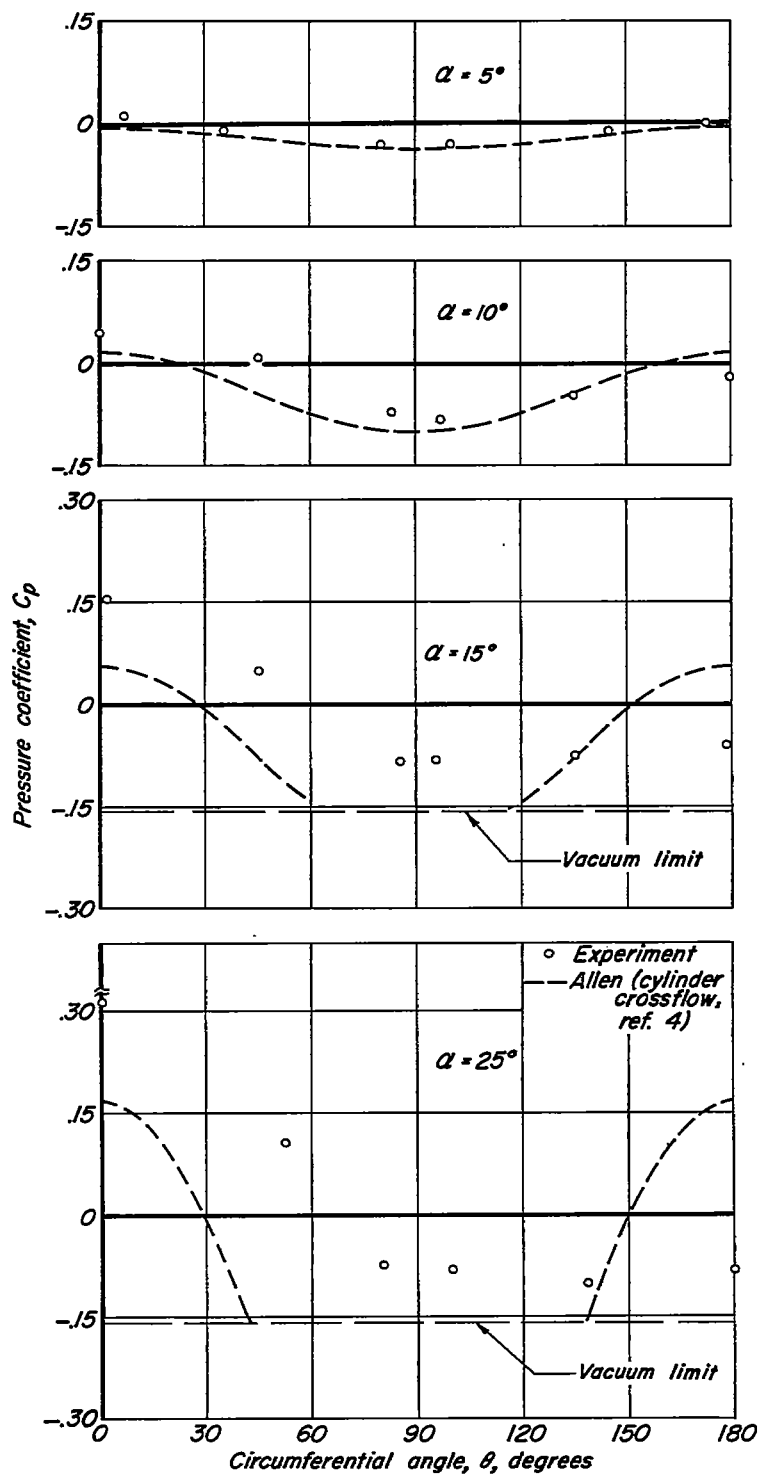


Figure 19.- Circumferential pressure distribution at midpoint of cylindrical afterbody at  $M_\infty = 3.02$ ,  $R = 8.6 \times 10^6$  per foot, and angles of attack to  $25^\circ$ ; comparison of theory and experiment.

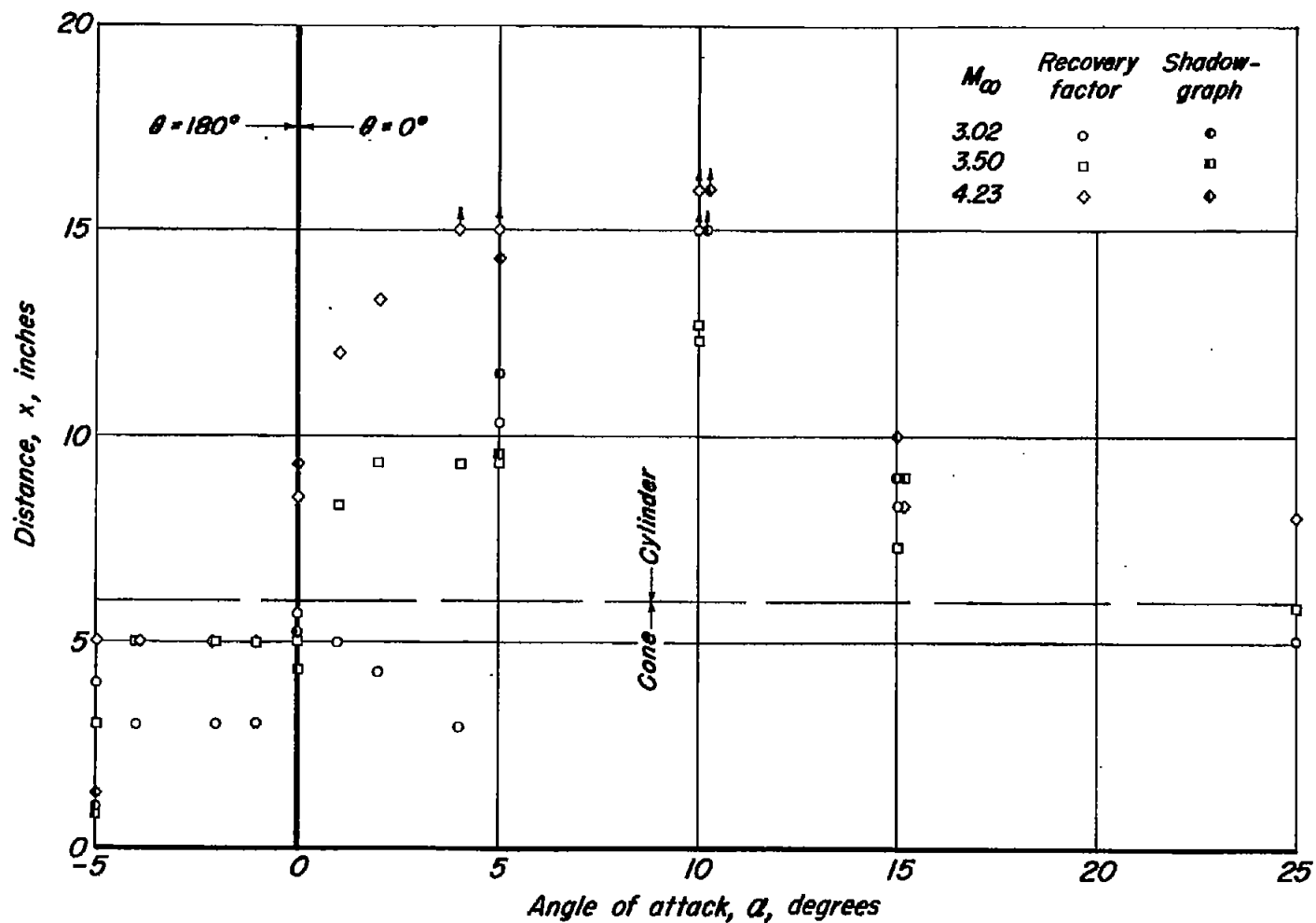


Figure 20.- Distance from tip of model to end of boundary-layer transition as a function of angle of attack.

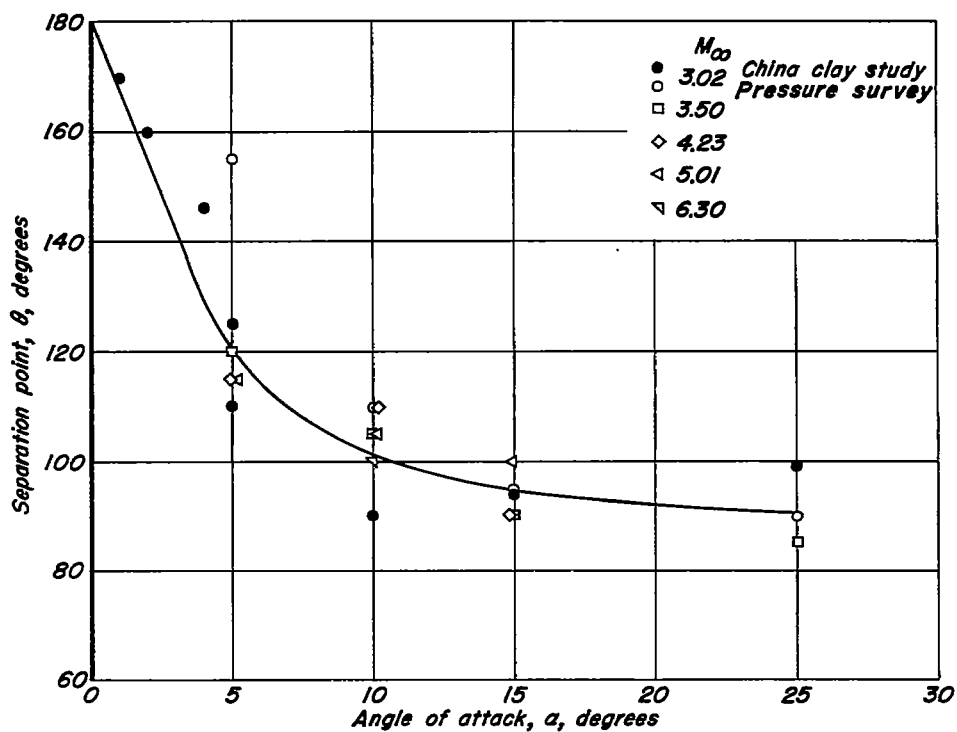


Figure 21.- Flow separation at midpoint of cylindrical afterbody as a function of angle of attack

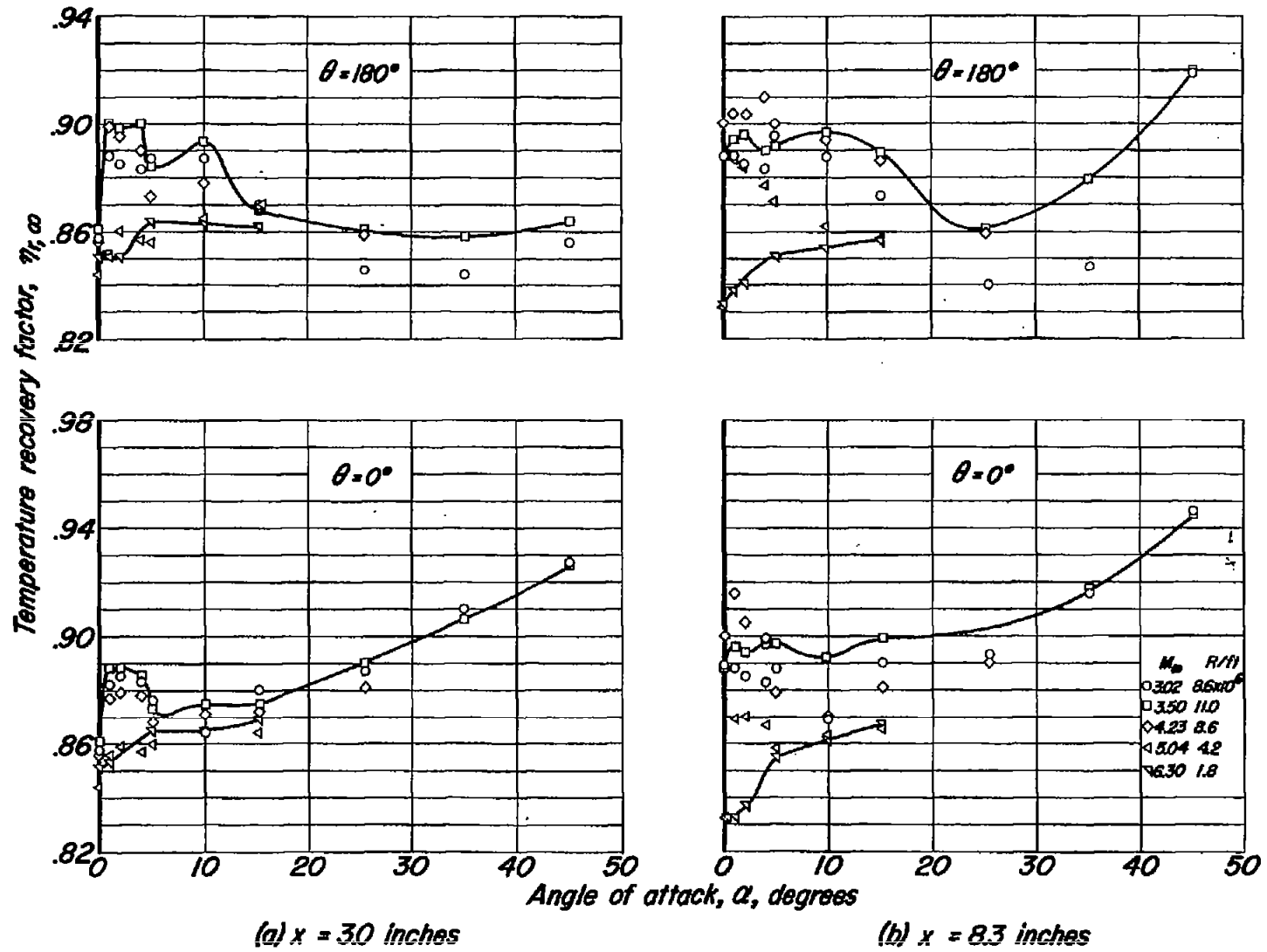
(a)  $x = 30$  inches(b)  $x = 8.3$  inches

Figure 22:- Recovery factor as a function of angle of attack.

CONFIDENTIAL

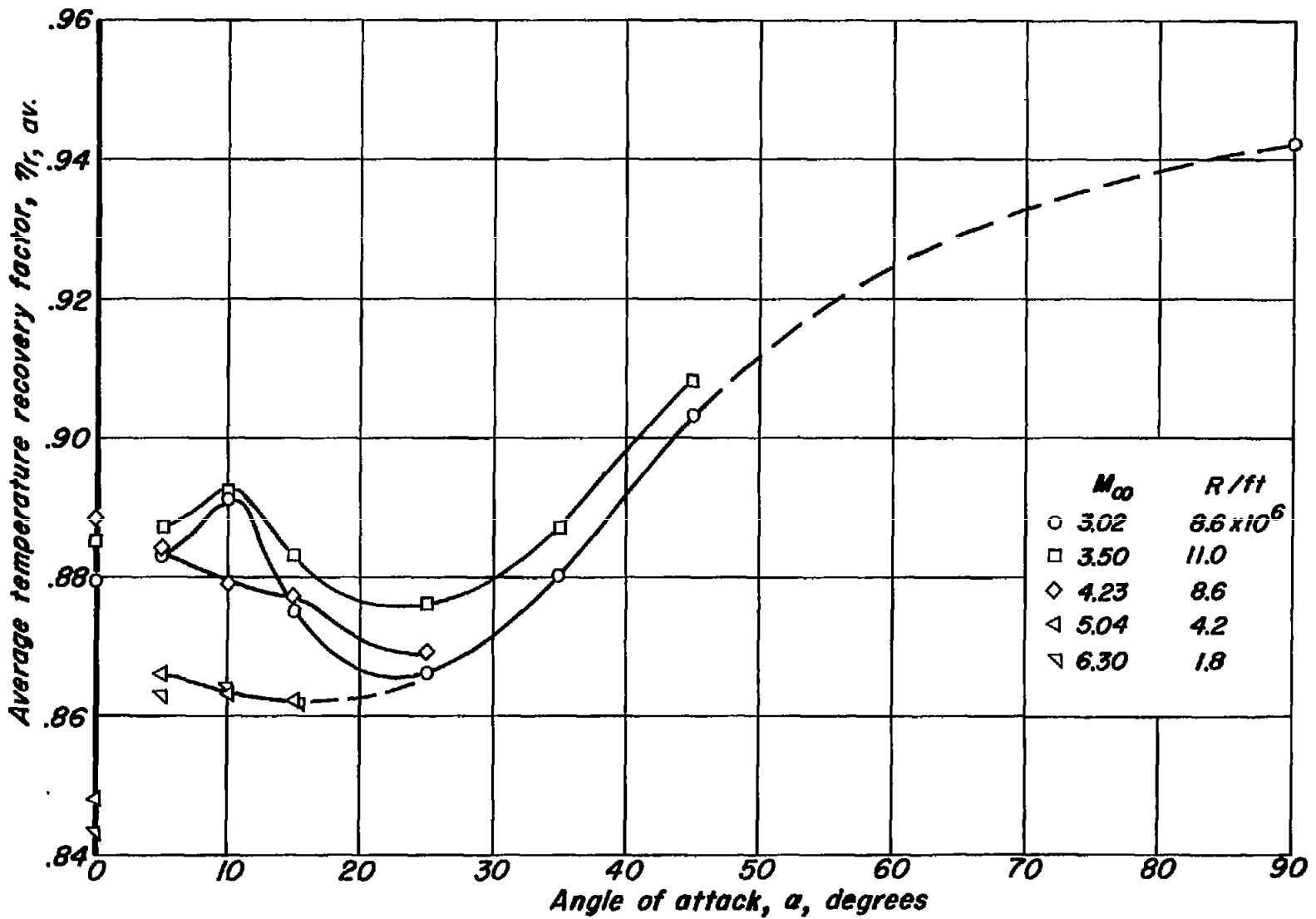


Figure 23.- Variation of average recovery factor with angle of attack.

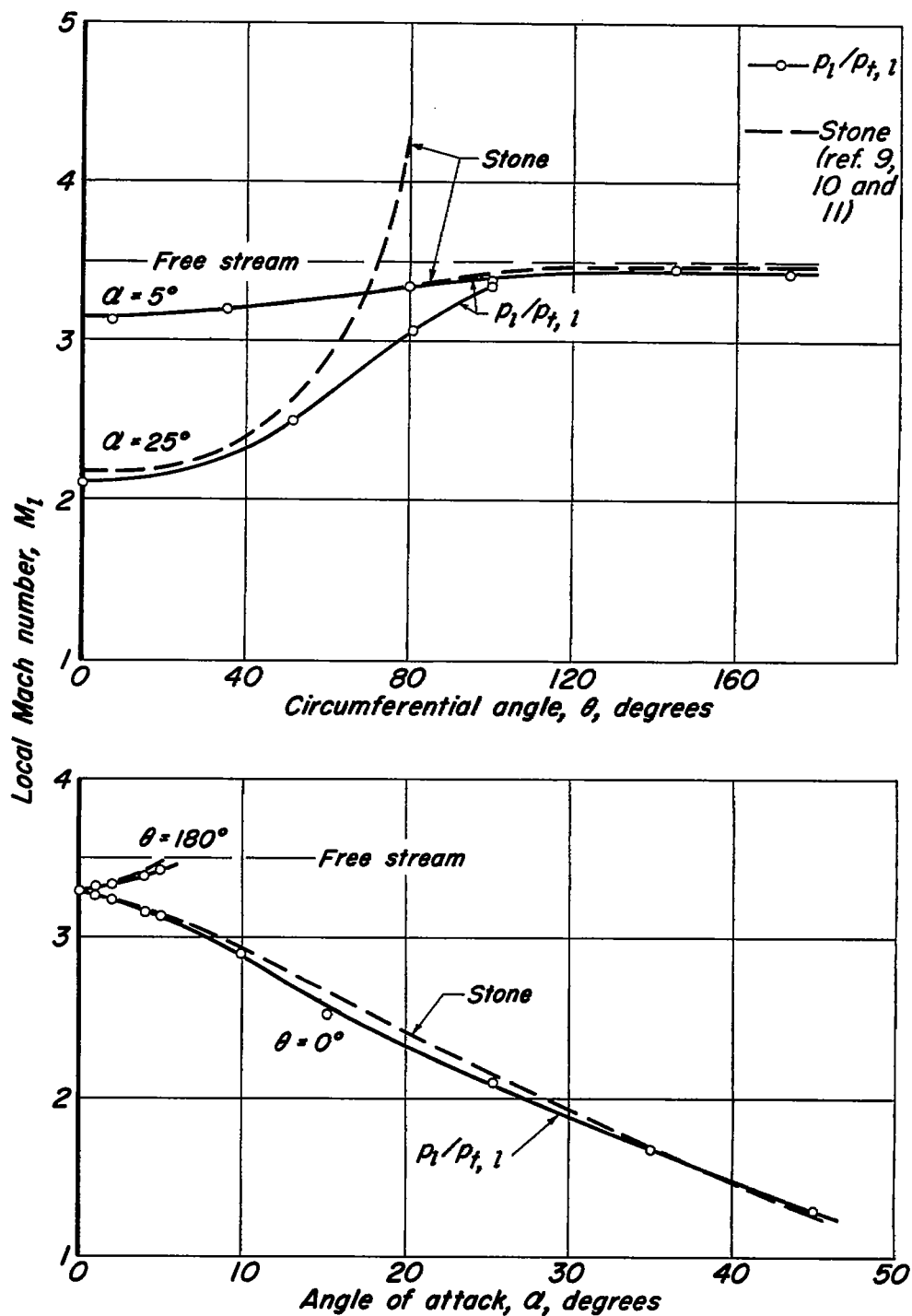


Figure 24.— Variation of local Mach number on cone with angle of attack and circumferential location,  $M_\infty = 3.50$ .

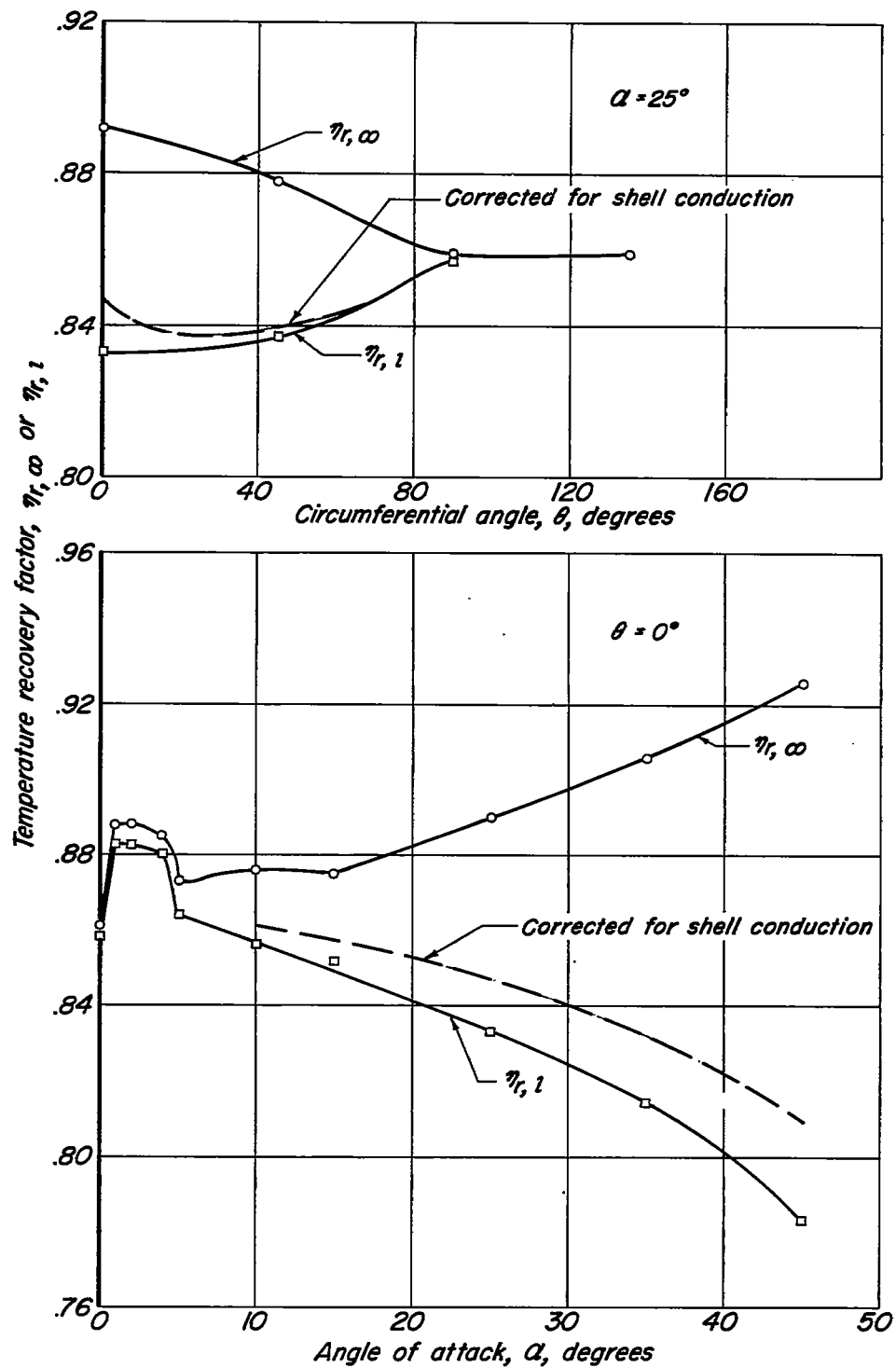


Figure 25.— Comparison of local and free-stream recovery factors at  $M_\infty = 3.50$ ,  $x = 3$  inches.



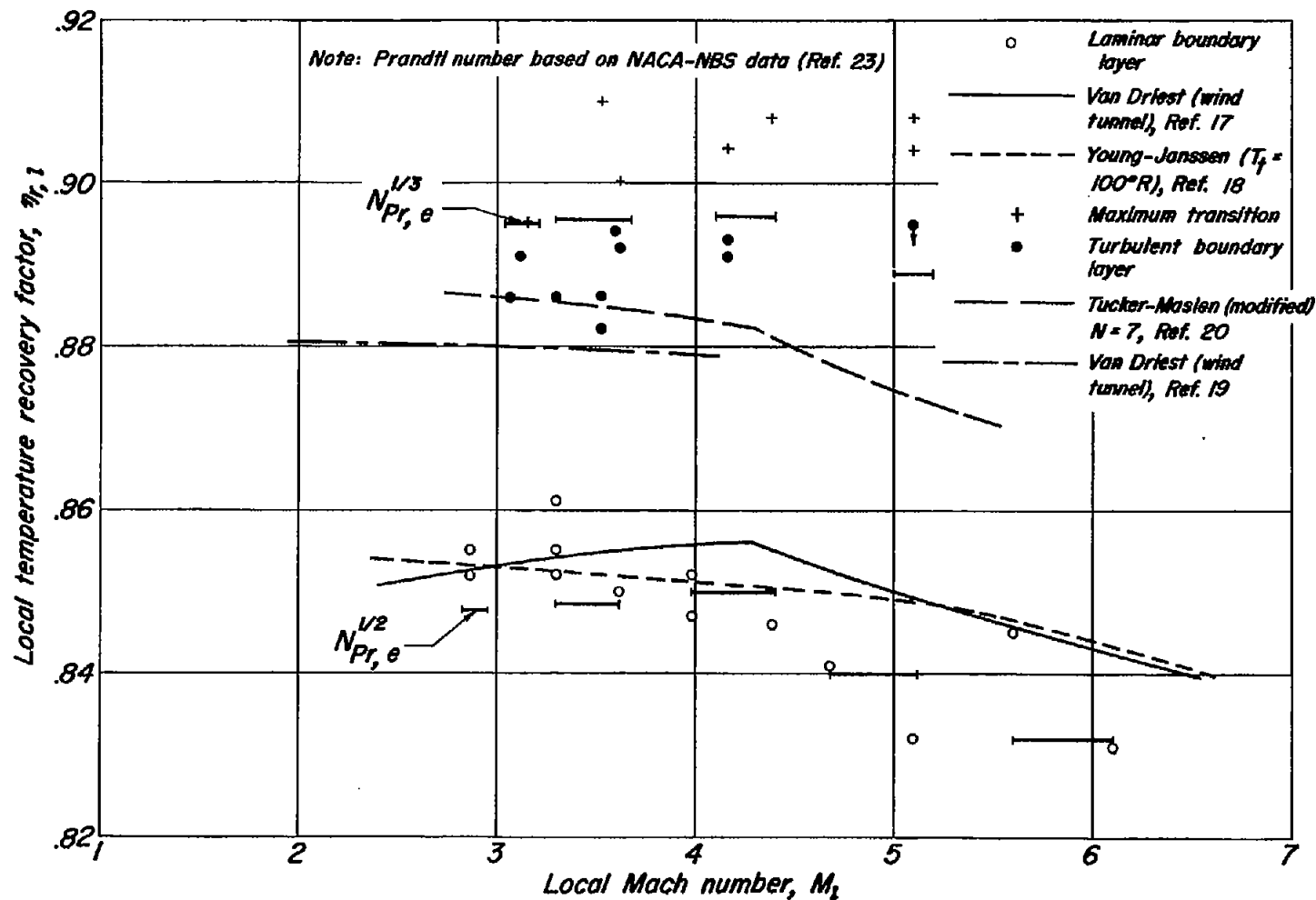


Figure 26.- Local recovery factor as a function of local Mach number at  $\alpha = 0^\circ$  and comparison with theory.